nature communications

Article

https://doi.org/10.1038/s41467-025-68175-5

A programmable ribozyme for RNA signal transduction

Received: 13 March 2025

Accepted: 22 December 2025

Mandy Yu Theng Lim[1,4], Chermaine Tan[1,4], Charannya Sozheesvari Subhramanyam[1,4], Shi Jie Teo[1], Louis DeFalco[2], Samuel Kevin Pasaribu[1], Chong Hui Koh[1], Dheeraj Rayamajhi[1], Jieying Chi[1], Shengnan Li[1], Keng Boon Wee[1], Sudipto Roy[1,3], Roland G. Huber[2] & Sherry Shiying Aw[1]

RNA detection applications can be augmented if a sensed RNA can be directly functionally transduced. However, there is no generalisable approach that allows an RNA trigger itself to directly activate diverse non-coding RNA effectors. Here, we report engineering of a programmable, RNA trigger-activated, dual-site self-cleaving ribozyme with modular sensing domain and cleavage product. This platform, UNlocked by Activating RNA (UNBAR), is entirely encoded within one RNA strand. The ribozyme can be designed to be almost completely inactive in absence of trigger, and to exhibit single-nucleotide trigger specificity. UNBAR ribozymes carry out cell-free sensing and protein-free amplification of microRNA and viral RNA sequences, and trigger-dependent release of ncRNA effectors sgRNA, shRNA and aptamer. We demonstrate RNA detection and functional transduction by a cleaved aptamer, whose fluorescence can be directly read out as a function of trigger RNA. We further engineer the ribozyme for function in cells, and demonstrate trigger-dependent regulation of CRISPR-Cas9 editing by sgRNA-embedded ribozymes in zebrafish embryos and human cells. UNBAR is a first-in-class modality with potential to be developed into a versatile platform for synthetic biology, diagnostics and gene regulation.

The logic of our genetic machinery has inspired biologists to use its components for precision applications in research, diagnostics and therapeutics. RNA is a particularly attractive material for engineering due to its diverse biological functions, which include post-transcriptional regulation resulting in gene repression (RNAi), gene expression (mRNA, circular RNA), translation activation (riboswitches) and reprogramming of translation (suppressor tRNA), as well as functioning as programmable guides for RNA and DNA effector complexes (CRISPR, ADAR).

The versatility of RNA has inspired engineering of RNA-sensing technologies based on various RNA modalities, including fluorescent aptamers that light up in response to RNA triggers[1,2], guide RNAs for CRISPR-Cas9-mediated gene editing modified to respond to RNA triggers or ligands via antisense blocking sequences and toehold-mediated strand displacement[3–15], gene regulatory machinery that can be targeted by microRNA (miRNA) (e.g. miRNA-directed Ago2 cleavage and release of sgRNA[16]) and miRNA-regulated Cas9 or other mRNA[17–20]. Switch-based approaches that utilise antisense blocking sequences on

---

[1]Institute of Molecular and Cell Biology (IMCB), Agency for Science, Technology and Research (A*STAR), Singapore, Singapore. [2]Bioinformatics Institute (BII), Agency for Science, Technology and Research (A*STAR), Singapore, Singapore. [3]Department of Paediatrics, National University of Singapore, Singapore, Singapore. [4]These authors contributed equally: Mandy Yu Theng Lim, Chermaine Tan, Charannya Sozheesvari Subhramanyam. e-mail: Sherry_Aw@a-star.edu.sg

the functional RNA are usually restricted in sequence due to their design, while methods based on sensing miRNA and/or recruitment of RNAi machinery are miRNA- and RNAi-specific. Methods that use RNA sensing to control designer mRNAs in cells have also been developed (e.g.[21–24] and reviewed in ref. 25). However, to our knowledge, no general approach currently exists that can convert a sensed RNA into a second, sequence-independent RNA signal, which can take the form of diverse non-coding RNA (ncRNA) effectors with specific functional outputs.

Ribozymes are RNA molecules with catalytic activity. Autocatalytic ribozymes have been used to precisely trim guide RNAs for CRISPR-Cas9 editing[26,27], and have been adapted for various cellular applications aimed at regulating mRNA function, including to enable stabilising RNA circularisation[28], to temporally control expression of AAV-delivered mRNAs[29], and to join up gene therapy payloads[30].

Here, we describe the development of an innovative modular RNA signal transduction platform based on a trigger-activated, conditional self-cleaving ribozyme. We iteratively engineer this ribozyme to comprise an RNA-sensing domain and two cleavage sites, between which can be embedded a releasable RNA cleavage product (e.g. a ncRNA effector). This is, to our knowledge, the first example of a single ribozyme that can cleave at two distinct sites to release almost any short RNA product of choice. The sequences of both the sensing domain and the cleavage product can be independently and modularly varied. Upon complementary binding of an RNA trigger, ribozyme cleavage is activated to release the embedded RNA cleavage product from ribozymes in cis and in trans. Hence, the ribozyme alone acts simultaneously as an RNA signal detector, transducer and amplifier. We employ 2D and 3D computational modelling techniques to understand how trigger binding activates ribozyme catalysis and permits the novel second-site cleavage we observed.

We develop ribozymes programmed to release short RNA, sgRNA, hairpin RNA and a fluorescent aptamer in an RNA sequence-specific, trigger-dependent manner in cell-free assays. These ribozymes can carry out protein-free RNA signal detection and functional transduction, as demonstrated by direct fluorescent readout of cleaved aptamer. We further engineer the ribozyme for function in cells by identifying variants that can cleave in cellular ionic conditions. We provide evidence that an sgRNA-embedded ribozyme can cleave to release the sgRNA in a trigger-dependent manner in cells to activate CRISPR-Cas9 editing. This versatile platform can potentially be explored for a range of synthetic biology and diagnostic applications.

Results

Engineering trigger-activated tandem ribozymes

We previously developed a miRNA sensor whose fluorescence is activated upon binding of a specific target miRNA[1], by altering the structure of the fluorescent RNA Spinach2[31,32], so that hybridisation of a target miRNA to its cognate sensor backbone is required for fluorescent complex stabilisation. We hypothesised that an analogous approach could be used to modify a catalytic RNA, reasoning that a ribozyme with sensing functions could be engineered from two or more RNA molecules if its stable catalytic conformation required reassembly of these RNAs. Specifically, one of these RNAs should comprise sequences complementary to a trigger RNA so that base-pairing between the ribozyme sensor and its trigger RNA would reconstitute an active ribozyme. We further hypothesised that tandem linkage of two such ribozymes could result in trigger-activated self-cleavage at two sites and release of an embedded RNA molecule from the tandem ribozymes, allowing for signal amplification if one trigger could activate self-cleavage of multiple ribozymes.

After considering the structural characteristics of various ribozymes, we selected the hairpin ribozyme (HpRz)[33–36] as a proof-of-concept based on two observations. First, previous studies have shown that two HpRzs linked in tandem exhibit dual cleavage, releasing a cleavage product[37,38]. Second, mutagenesis studies of the well-studied HpRz structure revealed the presence of a stem structure, helix 4 (H4), which is structurally required for ribozyme catalysis but whose sequence could be varied[39]. We hypothesised that self-cleaving activity could be assembled from several RNA molecules coming together at H4 to reconstitute HpRz structures. The HpRz comprises two independently folding stems A and B, each consisting of a loop containing key catalytic nucleotides, flanked by two helices (H1–H4) (Fig. 1A). The two loops dock prior to cleavage, and A_{38} and G_8 are critical to formation of the transition state[40–43]. The phosphodiester cleavage reaction then occurs between the N_{-1} and guanine (G_{+1}) nucleotides in loop A (Fig. 1A, black arrows). The sequence requirement at the cleavage site has been systematically studied; sequences with activity >20% of wild-type[35] are shown in Fig. 1A.

Fig. 1Bi shows a schematic of our original design approach. Two HpRzs, both modified to contain sequences complementary to a trigger miRNA, are arranged in tandem, one in a wild-type configuration ('right' side) and the other in a reverse-joined configuration ('left' side)[37,38]. In the absence of an intact H4[39] and without the trigger RNA, loop B was predicted to be conformationally unstable and hence unable to fold into a catalytically active conformation. The binding of the RNA trigger is predicted to stabilise loop B, activating cleavage and product release. This strategy required the original tandem-linked ribozymes[37,38] (Fig. 1Bii) to undergo three modifications (Fig. 1Biii–v). First, we would circularly permute the structure so that H4 would no longer be a closed stem loop; instead, the 5′ and 3′ ends would reside within both H4s (Fig. 1Biii; different junction configurations are possible). The tandem-linked ribozymes would consist of two strands, one containing the cleavage sites and cleavage product (strand 1; S1) and the second comprising a non-cleaved complementary strand (strand 2; S2). Next, we would introduce two sequence-variable stem loops that branch off from both H4s (IN-form; Fig. 1Biv), mimicking the structure formed by the binding of a trigger. Finally, we would assemble self-cleaving tandem ribozymes from three RNAs (S1, S2 and trigger RNA) that are sequence-complementary at the new branched H4s (OUT-form; Fig. 1Bv). Such a ribozyme is predicted to produce several different fragments when cleaved (Fig. 1C): the S2 strand (S2), the full-length S1 strand (FL), a 'left'-cleaved fragment that includes the cleavage product (R + C), a 'right'-cleaved fragment that includes the cleavage product (C + L), a 'left'-cleaved fragment without the cleavage product (L), a 'right'-cleaved fragment without the cleavage product (R), and finally, the dual-cleaved product (C)(Fig. 1C). We systematically tested the feasibility of this strategy.

We selected as a trigger the *Drosophila* microRNA *bantam-5p* (*ban-5p*), which could be effectively sensed by an analogous sensing domain[1]. As an example cleavage product, we chose a 29-nucleotide (nt) RNA (29nt-clvRNA). The first step was to circularly permute the tandem structure (Fig. 1Biii); this retained self-cleavage activity to release the embedded 29-nt cleavage product (Supplementary Fig. 1A). For the trigger-activated cleavage strategy to work, it is important that cleavage is inhibited by destabilising H4; indeed, while ribozymes with an 8 bp H4 released the cleavage product, shortening this helix (and thereby reducing its stability) reduced product release (Supplementary Fig. 1A).

The initial designs incorporated a 3-way junction (3WJ) in an HHH configuration (Fig. 1Biii and Supplementary Fig. 1Bi)[44], and dual-cleavage activity was low (Supplementary Fig. 1A). We took two approaches to boost cleavage. First, we tested alternative junctional configurations—2WJ (Supplementary Fig. 1Bii), 3WJ (HHS_4H) (Supplementary Fig. 1Biii) or 4WJ (Supplementary Fig. 1Biv)—that were previously shown to cleave better than the 3WJ (HHH)[44]. In addition, since re-ligation rates increase when the cleaved product is highly complementary within H1[45], we varied the degree of base-pairing between the cleavage product and S2. 3WJ (HHS_4H) and 4WJ unpaired at

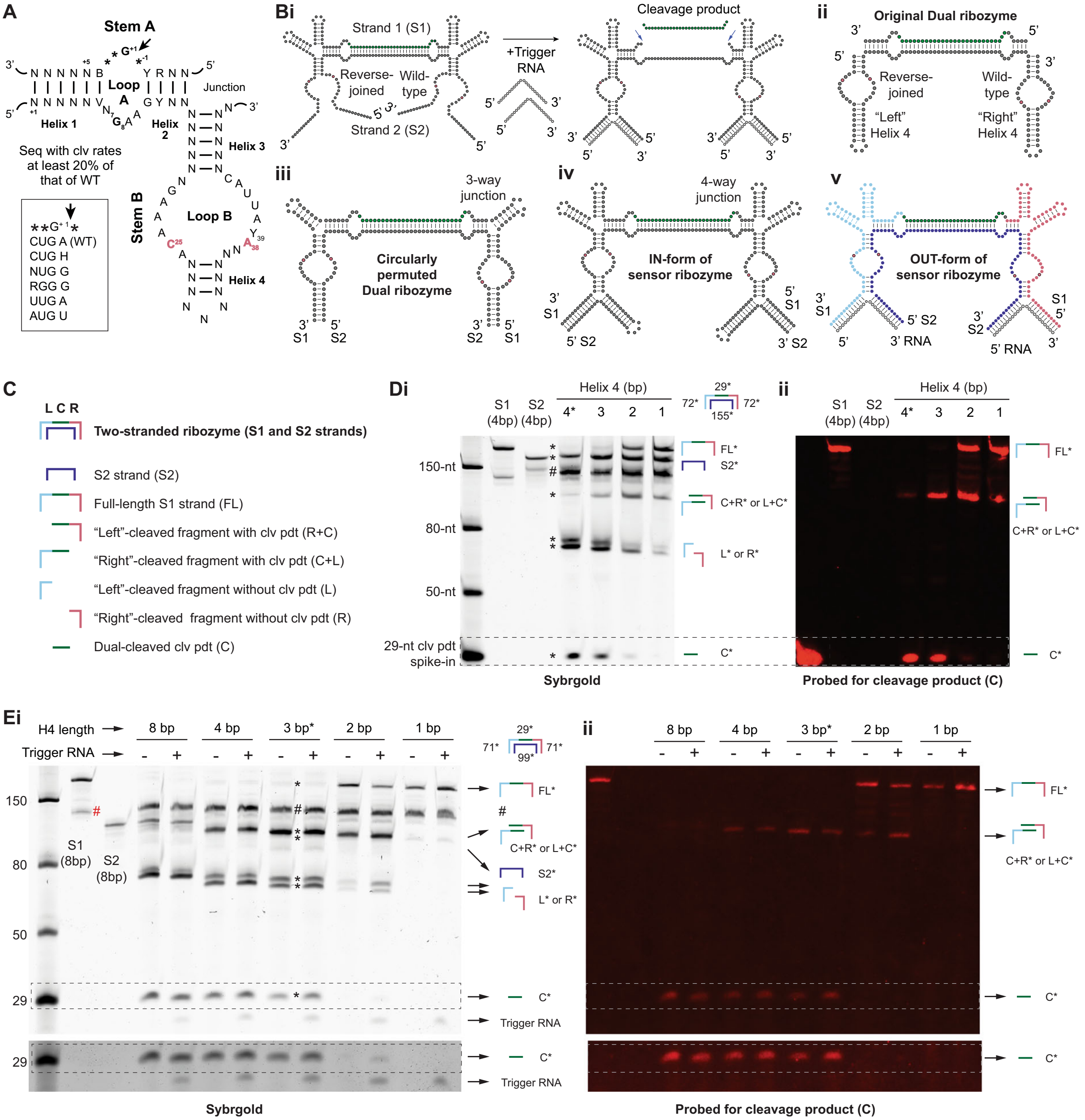

Fig. 1 | Development of tandem-linked self-cleaving ribozymes with two trigger-binding domains. A A representative hairpin ribozyme, numbered by convention. In the substrate strand, the arrow marks the cleavage site between the N_{-1} and G_{+1}. In the ribozyme strand, numbering is organised around G_8 in loop A. A_{38} and C_{25} are key catalytic nucleotides in loop B. 5′-*G**-3′ spans the cleavage site, and sequences with cleavage activity >20% of the wild-type are boxed (adapted from ref. 35 and abbreviated according to IUPAC code). **B**(i) Design strategy of RNA trigger-activated self-cleaving tandem ribozymes that release an embedded RNA cleavage product. (ii) Original tandem ribozymes (adapted from ref. 37). (iii) Circularly permuted tandem ribozymes. (iv) IN-form of self-cleaving sensor tandem ribozymes, where the RNA trigger is built into the ribozyme. (v) OUT-form of self-cleaving sensor tandem ribozymes, where the trigger RNA is separated from the ribozyme. Colours used for each cleaved fragment are consistent with the stick cartoons that label the fragments on the gels and blots, as detailed in (**C**). **C** Nomenclature for each fragment that can result from cleavage of tandem ribozymes. Colours are consistent with Fig. 1Bv. **D**(i) Gel of cleavage assays and (ii) Northern blot of the same gel probed for 29-nt cleavage product, of *ban-5p*-triggered IN-form tandem ribozymes with varying H4 length. Asterisks label bands corresponding to predicted cleavage products for the 4 bp H4 ribozyme. Ribozyme stick cartoons are coloured according to Figure 1Bv. These data demonstrate that an IN-form of sensor tandem ribozymes release substantial cleavage product when helix 4 (H4) is at least 3 bp long. **E**(i) Gel of cleavage assays and (ii) Northern blot of the same gel probed for 29-nt cleavage product, of *ban-5p*-triggered OUT-form tandem ribozymes with varying H4 length. Asterisks label bands corresponding to predicted cleavage products for 8 bp H4 tandem ribozymes. Hashtags indicate non-specific in vitro transcription products that are probe-negative. These data demonstrate that separation of trigger from the ribozyme IN-form allows for OUT-form, RNA trigger-activated tandem ribozymes. See Supplementary Fig. 1F for quantification of cleavage. Ribozyme stick cartoons are coloured according to (**B**(v), **C**).

H1 showed the highest amounts of dual-cleaved cleavage product (Supplementary Fig. 1Bv). However, fully unpaired H1 resulted in unexpected bands (Supplementary Fig. 1Bv), perhaps due to alternative ribozyme folding. Therefore, we partially restored complementarity to the 4WJ (HHHS$_2$H) (Supplementary Fig. 1C). A configuration of two paired nucleotides alternating with three or four unpaired nucleotides was effective at releasing the cleavage product (Supplementary Fig. 1C, configuration #5).

Next, we introduced branched stems into H4 to mimic an RNA-binding trigger region (Trigger-IN form, where the trigger RNA forms part of the ribozyme; Fig. 1Biv). We used the optimised 4WJ tandem ribozymes with alternating base-pair configuration (Supplementary Fig. 1C, #5). As H4 longer than 4 bp released dual-cleaved product in the absence of trigger (Supplementary Fig. 1A), we tested H4 of 1 to 4 bp (Supplementary Fig. 1D). IN-form ribozymes could self-cleave S1 to release substantial 29-nt cleavage product when H4 was at least 3 bp long (Fig. 1Di), with increased H4 length associated with greater product release (Supplementary Fig. 1E). This was corroborated using a probe for 29nt-clvRNA to label S1 and cleavage products comprising the 29-nt (Fig. 1Dii). Therefore, our combined modifications—circularly permuting the tandem ribozymes, reducing complementarity of the cleavage product, introducing a 4-way junction, and shortening helix 4 and altering it to be complementary to a trigger RNA—allowed the possibility of trigger-activated tandem ribozymes.

The sequence of the trigger region replacing H4 could be varied, allowing us to encode sequences complementary to trigger RNAs into the ribozymes. We therefore hypothesised that we could reconstitute ribozyme activity from three RNAs: a two-strand tandem-ribozyme with *ban-5p*-binding domain (OUT-form, Fig. 1Bv) and a short RNA (*ban-5p*). In the OUT-form, when H4 was 1–2 bp in length, the ribozyme released little dual-cleaved product even in the presence of trigger, and substantial S1 remained uncleaved (Fig. 1E and Supplementary Fig. 1F). A ribozyme with H4 of 3 bp released more cleavage product with the cognate trigger vs. a non-specific control trigger, and its corresponding A38mut catalytic mutant ribozyme did not cleave (Supplementary Fig. 1Gi; $p < 0.05$). Increasing H4 to 8 bp led to high background cleavage in the absence of trigger (Fig. 1Ei and Supplementary Fig. 1F), and a probe for the 29nt-clvRNA showed that cleavage activity correlated with H4 length (Fig. 1Eii). A second ribozyme, triggered by miRNA *hsa-let-7f*, also released a cleavage product in a trigger-dependent and cleavage-dependent manner (Supplementary Fig. 1H; $p < 0.05$). These data show that we have developed a tandem ribozyme structure with two cleavage sites, two loops B and two trigger-binding domains, which is activated by trigger RNA to release an embedded RNA cleavage product.

Development of a programmable dual-site single-stranded ribozyme

To understand the cleavage mechanism of tandem ribozymes, we mutated catalytic nucleotides in each loop B. A_{38} is a critical nucleobase that stabilises the transition state during catalysis[40–43,46] (Fig. 1A), and its mutation abolishes cleavage[47]. To our surprise, $A_{38}U$ mutation in either the 'right' wild-type or the 'left' reverse-joined loop B did not substantially reduce release of the cleavage product, and mutation of both was required to abolish cleavage (Fig. 2A and Supplementary Fig. 2A). This suggested that either single loop B was sufficient for dual cleavage.

To investigate this further, we designed ribozymes with a single wild-type loop B, as we reasoned that this conformation could be rationally optimised based on the abundant functional studies that have been carried out on this canonical structure (Fig. 2B). This ribozyme could now be encoded by a single strand of RNA, which, in a cleavage assay, would be predicted to produce: the full-length ribozyme (FL), a proximal-cleaved fragment that includes the cleavage product and distal fragment (C + D) a distal-cleaved fragment that includes the proximal fragment and cleavage product (P + C), a distal-cleaved fragment without the cleavage product (D), a proximal-cleaved fragment without the cleavage product (P), and finally, the dual-cleaved product (C)(Fig. 2Bii). Single-loop B ribozymes triggered by miRNAs (*hsa-mir-451a, dme-mir-184*, *dme-mir-252, dme-mir-263a* or *hsa-let-7f*) or by fragments of the E-gene and Orf1ab transcripts of the SARS-CoV-2 genome could all self-cleave at both cleavage sites to release the cleavage product (Fig. 2Ci and Supplementary Fig. 2Bi). This confirms that one loop B is sufficient for dual cleavage. $A_{38}U$ mutation in the single loop B abolished cleavage (Fig. 2C). This is, to our knowledge, the first example of a single HpRz capable of cleaving at two different cleavage loops, a phenomenon not previously described. Henceforth, ribozymes are named based on their trigger (T) RNA and cleavage (Cl) product; e.g., a ribozyme triggered by RNA *ban-5p* to cleave out a 29-nt cleavage product is named T-*ban-5p*_Cl-29nt-clvRNA.

Even though we observed dual cleavage of the single-loop B ribozymes, cleavage appeared to be trigger-independent (Fig. 2Cii, $p > 0.05$; and Supplementary Fig. 2Bii). To improve trigger-activated cleavage, we aimed to identify the optimal length and sequence for the H4 stem, which we predicted would function as a trigger-responsive communication module (CM)[48,49]. Ribozymes with H4 > 5 bp cleaved in a trigger-independent manner, while one with H4 = 2 bp did not release dual-cleaved product even in the presence of trigger (Fig. 2D). We systematically tested various CMs of 2 and 3 bp and identified two 3 bp motifs, 5′-ACG/CGU-3′ (3bp-v1) and 5′-ACG/CGA-3′ (3bp-v2), which greatly improved the signal-to-noise ratio of E-gene-triggered ribozymes (Fig. 2D). We tested the same panel of CMs for two other different trigger RNAs, *mir-451a* and SARS-CoV-2 S-gene, and found that 3bp-v1 and 3bp-v2 CMs also improve ribozymes triggered by these different RNAs (Supplementary Fig. 2C). We named this trigger-activated, single-stranded dual-site self-cleaving ribozyme platform: UNlocked By Activating RNA (UNBAR).

Our data show that cleavage can occur at a second site distal to the canonical (proximal) loop A (illustrated in Fig. 2B). Such dual-cleaving activity at separate cleavage loops has not, to our knowledge, been previously observed in any natural or engineered ribozyme and was unexpected here, as ribozymes fold into specific conformations for catalysis. Since loop A docks with loop B prior to cleavage, and G_8 in loop A is critical for stabilising the transition state[41–43], distal cleavage could occur via: (1) conformational rearrangement and 'sliding' of the distal G_{+1} cleavage site onto the proximal G_8[50], followed by canonical HpRz docking between loop B and proximal loop A; or (2) a novel docking event between loop B and the distal loop A. Mutation of G_8 at the distal loop A would affect cleavage at the distal G_{+1} in the second, but not the first, scenario. When we mutated G_8 in either or both loops A, we observed that the distal G_8 was essential for cleavage at the distal site but not for the proximal site, and vice versa (Fig. 2E). Therefore, distal cleavage occurs via a novel docking interaction between loop B and distal loop A.

Protein-free RNA signal transduction and amplification

Many methods for RNA detection require signal amplification to enhance the turn-on signal, or the fold-increase in detected signal of a target RNA compared to background. For example, in RT-qPCR, RNA is first copied into complementary DNA (cDNA) by enzyme-mediated reverse transcription, and the cDNA is subsequently amplified by gene-specific primers. Of note, this copied cDNA sequence is invariable as it depends on the RNA template. Therefore, we next asked whether UNBAR ribozymes alone could directly transduce one sensed trigger into amplified release of multiple copies of a sequence-independent RNA cleavage product. Keeping T-E-gene_Cl-29nt-clvRNA ribozyme concentration constant while increasing trigger RNA concentration, we observed that the cleavage product had a maximum turn-on signal of at least ~55-fold in presence vs. absence of trigger (Fig. 2F). To determine whether one trigger could cause amplified release of multiple cleavage products, we kept trigger concentration constant while increasing ribozyme concentration. We observed that when trigger amount is kept constant (50 nM), the amount of cleaved 29-nt cleavage product increases as more ribozyme is added (boxed region in Fig. 2G). At the lowest concentration (200 nM) of ribozyme, the amount of cleavage product released relative to the fixed amount of trigger was about 1:1. As more ribozyme is added, the amount of cleavage product

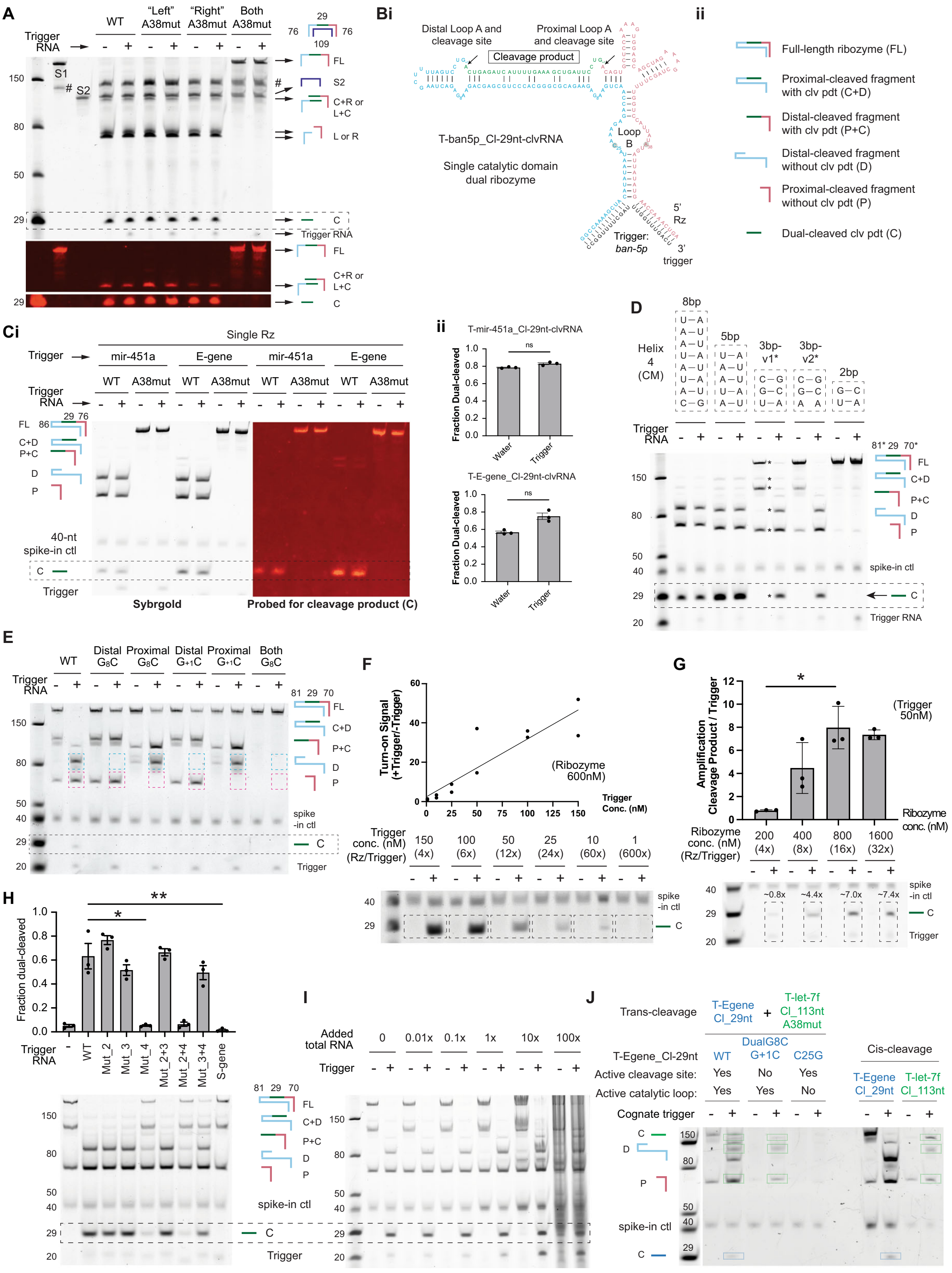

released from the self-cleaving ribozyme gradually exceeds the fixed amount of trigger, demonstrating that the original trigger signal has been amplified into released cleavage product. Quantification of the amount of cleavage product vs. trigger showed that the ribozyme exhibits up to ~7.4-fold amplification at 16-fold more ribozyme than trigger ($p < 0.05$)(Fig. 2G). Hence, a trigger RNA can cause the release of multiple cleavage products with programmable sequence, allowing the ribozyme to act as a protein-free signal detector, transducer and sequence-independent amplifier.

We next investigated the specificity of UNBAR ribozymes by introducing sequence changes into the test/trigger RNA (Fig. 2H; sequences used are shown in Supplementary Fig. 2D). An unrelated RNA (SARS-CoV-2 S-gene fragment) was unable to trigger cleavage product release by T-Egene_Cl-29nt-clvRNA ($p < 0.01$). The effects of single-nucleotide mismatches depended on their locations, with position 4 (from the 5′ end) reducing cleavage product release by ~90% ($p < 0.05$)(Fig. 2H). These results suggest that UNBAR ribozymes can be optimised to distinguish between similar trigger sequences. For

Fig. 2 | Optimised single-stranded UNBAR ribozymes exhibit sequence-specific RNA-triggered dual-self-cleavage to transduce and amplify RNA signals in complex mixtures. A Cleavage assays of *ban-5p*-triggered tandem ribozymes with an $A_{38}U$ mutation at either or both loops B demonstrate that one loop B is sufficient for dual cleavage. Top: Gel of cleavage assays of the indicated ribozymes. Bottom: Northern blot of the same gel probed for the 29-nt cleavage product. Hashtags indicate non-specific in vitro transcription products that were probe-negative. Also see Supplementary Fig. 2A for quantification. **B**(i) T-*ban-5p*_Cl-29nt-clvRNA ribozyme with dual cleavage sites and a single wildtype loop B. Colours used for each cleaved fragment are consistent with (ii). (ii) Nomenclature for each fragment that can result from cleavage of single-loop ribozymes. Colours are consistent with (**B**)i. **C**(i) Cleavage assays of single ribozymes with dual cleavage sites and a single wildtype loop B triggered by *hsa-mir-451* or SARS-CoV-2 E-gene fragment. Both ribozymes can cleave at two cleavage sites to release the embedded 29-nt cleavage product. Panel at right shows northern blot of the same gel probed for the 29-nt product. (ii) Densitometry of the fraction dual-cleaved in (i) shows no significant increase in release of cleavage product with trigger. **D** Cleavage assays showing optimisation of the H4 communication module in T-E-gene_Cl-29nt-clvRNA and identification of 3 bp motifs that improve the signal-to-noise ratio. Asterisks mark bands corresponding to predicted cleavage products for the 3 bp ribozymes. **E** Cleavage assays of ribozymes mutated at either or both of the proximal and distal G_8 docking nucleotides in T-E-gene_Cl-29nt-clvRNA shows that cleavage at the distal site requires the distal G_8 and cleavage at the proximal site requires the proximal G_8. **F** Cleavage assays of 600nM T-E-gene_Cl-29nt-clvRNA with varying concentration of E-gene trigger show increasing cleavage with increasing trigger concentration, with a maximum turn-on signal of at least ~55-fold. Data represents two biological replicates. **G** Cleavage assays of T-E-gene_Cl-29nt-clvRNA show that cleavage product release increases with increasing ribozyme, at constant 50 nM of trigger RNA. This demonstrates that the original trigger amount has been transduced into amplified amount of cleavage product. Chart plots the ratio of dual-cleaved product over the constant trigger amount ($*p = 0.0269$). **H** Testing mutant variants of E-gene trigger against T-E-gene_Cl-29nt-clvRNA shows that UNBAR ribozymes can distinguish between unrelated and closely related trigger RNAs with 1–3 nt differences ($*p = 0.0369$; $**p = 0.0046$). Sequences of test triggers are shown in Supplementary Fig. 2D. **I** Cleavage assays carried in with excess mammalian cell RNA show that ribozymes can detect trigger RNA spiked into a mixture of at least 100-fold excess competing RNA. **J** Cleavage assays of two UNBAR ribozymes with different triggers and cleavage products in the same reaction, shows that a trigger-bound ribozyme with an active catalytic loop can trans-cleave a second, catalytically dead ribozyme to release its cleavage product. Ribozyme stick cartoons are coloured according to (**B**). Gel analyses for **C**ii, **G** and **H** present three biological replicates ($n = 3$) with error bars showing mean and SEM. Statistical significance was assessed by non-parametric one-way ANOVA (Friedman test) with Dunn's multiple comparisons test ($*** = p < 0.001$, $** = p < 0.01$, $* = p < 0.05$, ns $= p > 0.05$).

UNBAR ribozymes to be useful in mixed RNA samples, they should also identify their triggers within complex mixtures. We found that T-E-gene_Cl-29nt-clvRNA ribozyme could detect trigger RNA spiked into a mixture comprising 100-fold excess of competing mammalian cell RNA (Fig. 2I).

Finally, we asked whether an UNBAR ribozyme can dock with and cleave a cleavage site in a separate UNBAR ribozyme molecule (trans-cleavage). A wild-type T-E-gene_Cl-29nt-clvRNA ribozyme was incubated in a cleavage reaction with a second, catalytically inactive (A_{38} mutant) ribozyme triggered by a different RNA trigger (*let-7f*) to release a 113-nt cleavage product (T-let-7f _Cl-113nt-clvRNA_A38mut). When only E-gene fragment was provided in the cleavage reaction, we observed cleavage and release of both the short and long cleavage products, providing evidence that the E-gene-bound and activated ribozyme can dock upon and trans-cleave the catalytically inactive second ribozyme to release its long cleavage product (Fig. 2J). Mutations of the cleavage site $G_{+1}C$, G_8C in loop A and $C_{25}G$ in loop B of the E-gene-triggered ribozyme confirmed that a trigger-bound ribozyme can trans-cleave another UNBAR ribozyme as long as its loop B is catalytically active (Fig. 2J). Therefore, a trigger-bound UNBAR ribozyme can trans-cleave other, trigger-free ribozymes, potentially allowing signal amplification (Fig. 2G).

Computational modelling of ribozyme structural properties

An E-gene-triggered ribozyme with a 3 bp-v1 H4 exhibited substantially increased cleavage activity in the trigger-bound (+trigger) vs. trigger-free (−trigger) state (Fig. 2D). We used 2D and 3D computational modelling techniques to understand the effect of trigger binding on this ribozyme compared to other E-gene-triggered ribozymes with 2, 5 and 8 bp H4s. Combined *k*-means clustering of predicted ±trigger thermodynamic secondary structure ensembles of the 3 bp-v1 ribozyme showed marked reduction in conformational variability (fewer, more compact clusters) in +trigger vs. −trigger structures (Fig. 3A). Examination of predicted structures showed high probability base-pairing between trigger-binding arms and catalytically critical[33,38] and highly conserved[41] nucleotides A_{38} and C_{25} in the absence of trigger (Fig. 3B). This stable interaction likely creates an auto-inhibitory state with a significant energetic barrier to catalytic loop formation, offering a structural rationale for the limited background cleavage observed in the absence of trigger for the 3 bp-v1 ribozyme (Fig. 2D). High-affinity binding of trigger RNA releases the catalytic core residues (Fig. 3A, B). Although −trigger structures with +trigger homology could be found in predominantly +trigger clusters (Fig. 3A, B), these structures are outliers (±trigger ensembles are statistically different [$P \approx 0.05$], with low probability of overlap in Cartesian space). Trigger binding, therefore, shifts ensembles away from a diverse set of structures where A_{38} and C_{25} residues are "trapped" through association with the trigger arms and towards a defined set of conformations with greater catalytic potential. These conformational properties may underlie the low leakiness and high signal of the 3 bp-v1 ribozyme.

Lengthening H4 to 5 bp (Supplementary Fig. 3A) or 8bp (Fig. 3C, D) resulted in greater homology between −trigger and +trigger structures. For the 8 bp H4 construct, there was substantial overlap ($p \approx 0.61$) of pairwise distances between ensembles of ±trigger states (Fig. 3C); this was exemplified by their highly similar centroid structures (Fig. 3D). Hence, H4 formation appears important for stabilisation of the active catalytic loop. Without trigger, increased H4 length can shift ensembles towards an active conformation: 8 bp H4 -trigger structures exhibited intact H4 and ipsilateral A_{38} and C_{25} residues within a catalytic loop-like structure (Fig. 3D), similar to those observed in crystallography experiments[51]. Therefore, we next asked whether the probability of H4 formation correlated with experimental cleavage efficacy.

Ribozyme sequences with varying H4 lengths and in both ±trigger states were used to sample 100,000 secondary structures from the Boltzmann ensemble. Resulting statistical ensembles were searched for fully paired H4. Unsurprisingly, increasing H4 length corresponded with increasing probability of reconstituted H4: in the absence of trigger, ~79% of 8 bp H4 structures contained reconstituted H4 (similar to +trigger percentages) (Fig. 3E), while trigger-bound 2 bp H4 exhibited only ~0.31% H4 formation (Fig. 3E). Furthermore, ±trigger H4 reconstitution rates were predictive of the respective cleavage efficacies in cell-free assays (Fig. 2D), suggesting that H4 stability is integral to dual-site ribozyme activation. Therefore, an ideal H4 should not base-pair in the absence of a trigger but should stably form when a trigger is present.

To study the cleavage reaction at the distal site required analysis of UNBAR ribozymes in multiple cleaved states. We used 3D modelling and molecular dynamic simulation techniques to deduce the conformational preconditions that prompted the novel observation of distal site cleavage. A tertiary structure model derived from minimum free energy (MFE) secondary structure constraints was used to generate uncleaved and proximal site-cleaved (proximal G_{+1} phosphate removed) models. For each state, average A_{38}-G_{+1} distances to both

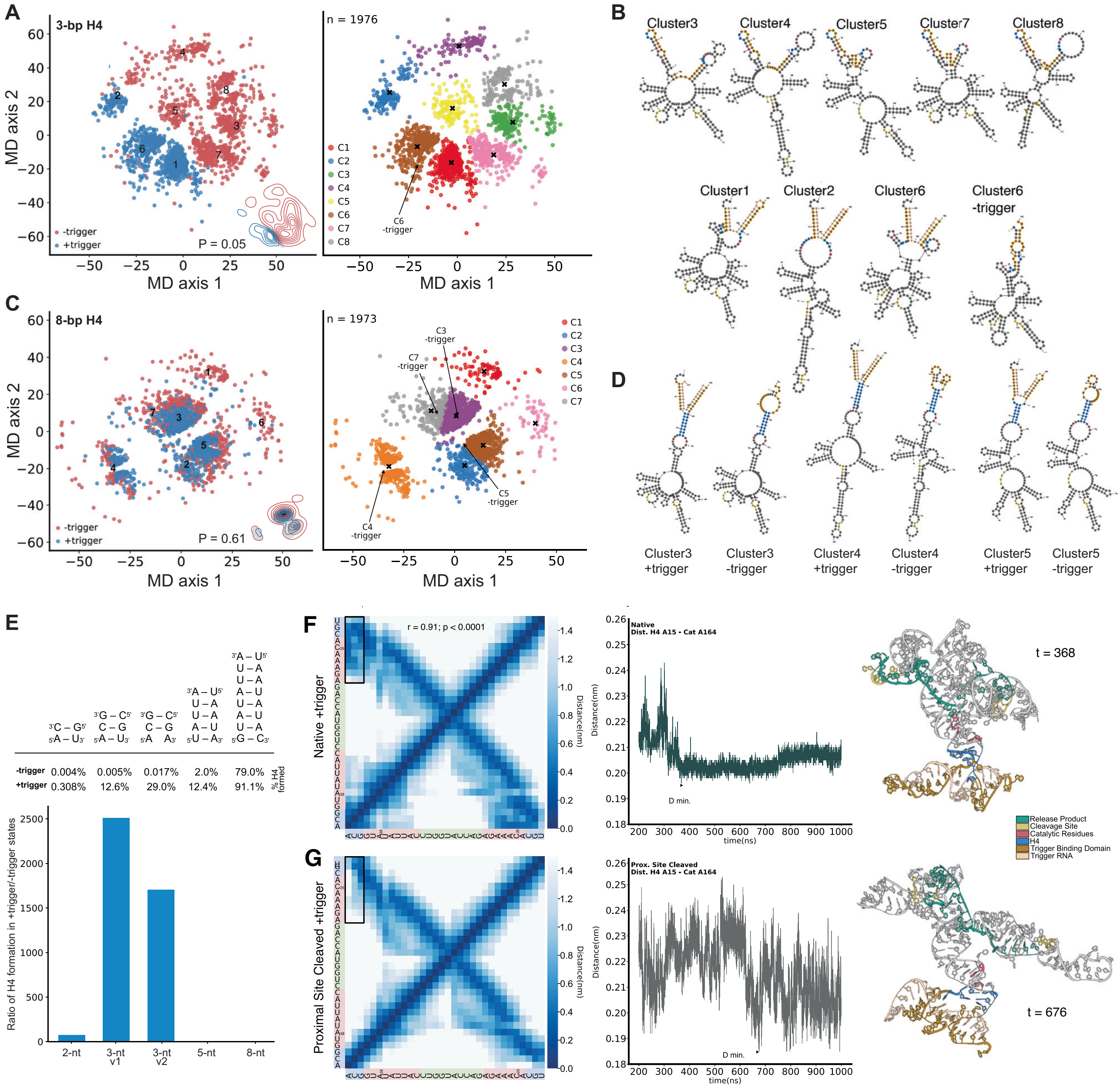

Fig. 3 | Optimal helix 4 sequences destabilise stem B in the trigger-free state but promote stability in the trigger-bound complex. Combined ±trigger *k*-means secondary structure clustering of the 3bp-v1 H4 (**A**) and 8bp H4 (**C**) UNBAR ribozymes. (Left) Embeddings are coloured according to trigger-bound or unbound states. (Right) Similar secondary structures are clustered together and marked by different colours. The geometric centre of each cluster is marked with an 'x'. Overlapping volume is determined as the sum of minimum volumes between either kernel at each position and reported as probability (P) between 0.0-1.0. **B**, **D** Centroid secondary structures for each cluster shown are those closest to 'x' as marked in (**A**, **C**). Structures are colour-coded as follows: H4 (blue); trigger-binding arms (brown); trigger (beige); cleavage sites (yellow); A_{38} and C_{25} (pink). **E** (Top) H4 sequence and secondary structure for 2 bp, 3 bp, 5 bp and 8 bp lengths and their prevalence in + and −trigger ensembles. (Bottom) Ratio of +trigger to −trigger reconstituted H4 as a function of helix length. **F** (Left) Contact map showing pairwise distances of stem B residues in an 'uncleaved' state over 1 μs of simulation time. (Centre) The distance time series of the nearest stem B nucleotide pair over 1 μs of simulation time (A_{15} is 5nt 5′ to A_{38}, and A_{164} is 2nt 5′ to C_{25}). (Right) 3D model of the uncleaved ribozyme at the time point of the minimum distance. (Pearson correlation coefficient ($r \approx 0.91$) between the pairwise base distances in 'native' and 'proximal site cleaved' ribozyme states; $p < 0.0001$ (parametric, two-sided t-test. One set of measurements were made for each ribozyme state). **G** Figures and analysis are identical to those described in F except in a 'proximal site cleaved' state.

sites were comparable and in a narrow range (~4.0-5.0 nm). This suggests that both sites are similarly accessible to the catalytic loop (Supplementary Fig. 3B), supporting dual-site cleavage.

Understanding the degree to which single-site cleavage affects ribozyme dynamics may help predict the structural context for subsequent cleavage. We measured pairwise distances of stem B residues over 1 μs (Fig. 3F). The distance between H4 and catalytic loop residues in the uncleaved simulation reached a minimum at around 368 ns with limited fluctuation thereafter, suggesting that the catalytic loop adopts a stable conformation before initial cleavage. After proximal-site cleavage, the H4-catalytic loop region appears less stable, as indicated by larger distance fluctuations between H4-catalytic loop residues throughout the entire simulation trajectory (Fig. 3G). Throughout the cleaved simulation, binding of trigger RNA helped to maintain catalytic loop integrity even after proximal-site cleavage, likely allowing exploration of conformations susceptible to distal site cleavage. This stability may be lost without trigger, trapping the ribozyme in a disordered, cleavage-resistant state.

Functional RNA as cleavage products: single guide RNA, hairpin RNA and an aptamer

To explore whether UNBAR ribozymes can transduce sensed RNA inputs into functional RNA outputs, we first asked whether RNA effectors with more complex secondary structures could be embedded as cleavage products. We engineered ribozymes that comprise a CRISPR single guide RNA (sgRNA; Fig. 4A), a short hairpin RNA (shRNA; Fig. 4B) or an aptamer (Red Broccoli[52]; Fig. 4C). To allow for cleavage (Fig. 1A), three and two nucleotides were left in the cleavage 'scars' at the 5′ and 3′ ends of the cleavage products, respectively. The functional relevance of the cleavage scars will depend on the nature of the cleavage product and require functional testing, which we carry out in the next section for a sgRNA-releasing ribozyme. A previous study found that a non-canonical N_3 in the catalytic loop can be compensated by mutation of A_7 in the wild-type cleavage loop to base-pair with N_3[53] (Supplementary Fig. 4Ai), a finding that we replicated (Supplementary Fig. 4Aii). This reduces cleavage scar limitations.

For these ribozymes (Fig. 4D–F), we chose *let-7f* as the trigger RNA. The *let-7* family is highly conserved, with *let-7f* one of its most abundantly expressed members (www.mirbase.org and ref. 54). The concentration of *let-7* in mouse mesenchymal stem cells was previously estimated at ~42,000 copies per cell or ~46 nM[55], which is within the range detectable by UNBAR ribozymes in our cell-free assays (>10 nM; Fig. 2F). In addition, there is data to suggest that at least 50% of *let-7a* is stably expressed but not bound to Ago[56]. We assayed T-let-7f_Cl-sgRNA, T-let-7f_Cl-shRNA and T-let-7f_Cl-Red-Broccoli for trigger-activated cleavage in cell-free assays, and observed substantially more cleavage product released in the presence of trigger than without (Fig. 4D–F). Quantitative analyses showed that no cleavage was observed with non-specific triggers for the sgRNA and shRNA ribozymes (Supplementary Fig. 4Bi, ii; $p < 0.05$) or with their respective non-cleaving catalytic mutants (Supplementary Fig. 4Bi, ii). The Red-Broccoli-releasing ribozyme also tended to show increased cleavage with specific trigger compared to non-specific trigger (Supplementary Fig. 4Biii). Therefore, UNBAR ribozymes can be triggered to release RNA with more complex structures, including sgRNA, shRNA and aptamers.

For a majority of these ribozymes, we observed background, trigger-independent cleavage at the site proximal to loop B (Figs. 2 and 4D–F). However, the distal site was not cleaved without trigger. We hypothesised that this was due to its increased distance from loop B. To test this, we lengthened H2 of T-let-7f_Cl-sgRNA from 4 bp to 8 and 12 bp (Supplementary Fig. 4Ai). This decreased trigger-independent cleavage at the proximal site (Supplementary Fig. 4Ci). We similarly altered the shRNA-embedded ribozyme and observed a comparable effect (Supplementary Fig. 4Cii). Since loops A and B dock prior to catalysis[41–43], we hypothesised that H3 length can also influence cleavage efficacy. Lengthening of H3 also decreased trigger-independent background cleavage at the proximal site (Supplementary Fig. 4D; we note that the larger shRNA ribozyme fragments occasionally migrate at larger sizes, likely due to dsRNA formation of the highly self-complementary fragments even in a denaturing gel). Therefore, helices 2 and 3 can be individually altered to refine cleavage regulation by the trigger RNA. This led us to ask whether we could identify an optimal combination of altered H2 and H3 that applies across different types of RNA cleavage products. We tested 30 combinations of helices 3 and 2, where H3 was varied from 2 to 7 bp and H2 was varied from 1 to 6 bp (Supplementary Fig. 4E). We found that a ribozyme with a 7 bp H3 paired with a 5 bp H2 (7H3, 5H2), as well as (6H3, 3H2), (5H3, 3H2), (4H3, 3H2), (3H3, 5H2) and (3H3, 3H2), showed strong trigger-dependent cleavage with minimal trigger-independent background cleavage (Fig. 4G). We then tested ribozymes embedded with other cleavage products with the best-performing helix combinations and found that (7H3, 5H2) and (5H3, 3H2) ribozymes cleaved with a high signal-to-noise ratio across modalities (Supplementary Fig. 4F).

Since UNBAR ribozymes can directly transduce detection of a trigger RNA into amplified release of a second RNA by self-cleavage (Fig. 2F, G), they have the potential to form a novel class of diagnostics. We hypothesised that RNA trigger-activated cleavage and signal amplification can be functionally read out if the cleavage product is a fluorescent aptamer, e.g. Broccoli[57] (Fig. 4Hi). To test this, we designed ribozymes triggered by a fragment of the SARS-CoV-2 E-gene, to self-cleave and release Broccoli (Fig. 4Hii). In-gel staining of cleavage assay products showed strong fluorescence only of the dual-cleaved Broccoli cleavage product (Fig. 4Ii), with increased dual cleavage and release of Broccoli as trigger concentration was increased (Fig. 4Iii). Increasing fluorescence with increasing trigger concentration could be detected on a plate reader, with turn-on signals of up to ~10-fold (up to 20-fold could potentially be reached with a higher concentration of ribozyme; Supplementary Fig. 4G) and sensitivity of at least 25 nM (Fig. 4J). Therefore, UNBAR ribozymes can be used to directly detect trigger RNAs, and transduce and report their concentration via fluorescence of the released aptamer cleavage product.

UNBAR function in cells

We next asked if UNBAR could function in cellular contexts by investigating whether the *let-7*f-triggered ribozyme embedded with an sgRNA against GFP (Fig. 4A) could regulate CRISPR-Cas9 editing. We tested this ribozyme in the zebrafish model, as l*et-7* is present in the early zebrafish embryo[58], and ribozyme-Cas9 ribonucleoprotein complexes can be directly microinjected into embryos. In fish, *let-7a*, *-c* and *-f* account for ~72% of *the let-7* miRNA family (www.mirbase.org). A *let-7f*-triggered ribozyme could distinguish *let-7b, let-7i* and *mir-98* from the rest of the *let-7f* family (Supplementary Fig. 5A), demonstrating that UNBAR ribozymes can be designed to distinguish between some members of related miRNA sequences. Injection of WT or catalytic mutant T-let-7f-Cl-sgRNA-GFP ribozymes with Cas9 protein into transgenic GFP[59] embryos led to strong GFP down-regulation in embryos injected with the WT ribozyme but not the mutant ribozyme ($p < 0.0001$; Supplementary Fig. 5B, C), demonstrating that ribozyme cleavage was required for editing.

We next used DNA fragment analysis to obtain a more quantitative measurement of editing levels. Injection of positive control $\text{sgRNA}^{\text{GFP}}$ with Cas9 protein led to high rates of editing at the target locus (~92%; Supplementary Fig. 5D). Injection of equimolar amounts of ribozyme T-let-7f_Cl-$\text{sgRNA}^{\text{GFP}}$ with Cas9 also led to robust editing, although ~50% lower than the sgRNA alone (Supplementary Fig. 5D), which could be due to incomplete dual-cleavage of the ribozyme within the embryo. To determine whether editing was trigger-dependent, we introduced a morpholino antisense inhibitor against *let-7f*. Compared to co-injection with a control inhibitor, co-injection of the *let-7f* inhibitor significantly reduced ribozyme-induced editing in the fish (Fig. 5A; $p < 0.0001$), although the presence of other members of the *let-7* family may result in incomplete inhibition. There was no difference in the survival rates of the *let-7f* vs. control inhibitor samples (80% vs. 75%, respectively). In cell-free assays, the inhibitor disrupted trigger-induced cleavage by a trigger-dependent ribozyme (Supplementary Fig. 5Ei), but did not disrupt cleavage of a non-trigger-dependent (auto-cleaving) ribozyme with an 8 bp H4 (Supplementary Fig. 5Eii), demonstrating that the inhibitor can compete with the ribozyme for the trigger, and that it inhibits ribozyme cleavage by trigger-binding rather than by disrupting overall ribozyme structure. These experiments provided evidence that UNBAR ribozymes can potentially regulate sgRNA function in a trigger-dependent manner in cellular contexts.

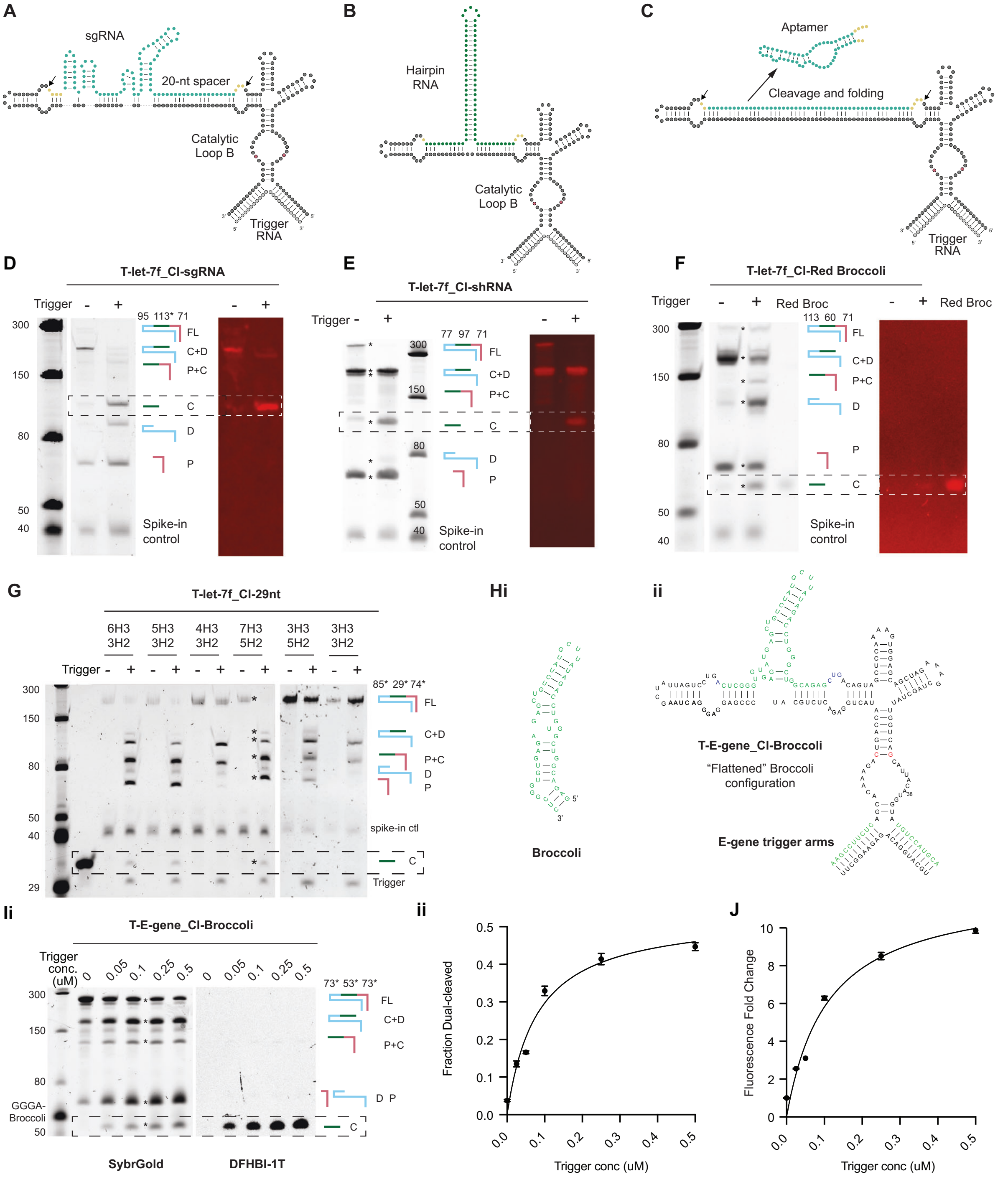

Fig. 4 | Various non-coding RNA can be embedded in and cleaved from UNBAR ribozymes in a trigger-dependent manner for RNA signal transduction. Cartoons of ribozymes that comprise an embedded single guide RNA (sgRNA) (**A**), a short hairpin RNA (shRNA) (**B**) and an aptamer (Red Broccoli) (**C**). Cartoons are not drawn to scale; complementarity and lengths of various regions may vary. Cleavage assays for ribozymes T-let-7f_Cl-sgRNA^{GFP} (**D**), T-let-7f_Cl-shRNA^{GFP} (**E**) and T-let-7f_Cl-Red Broccoli (**F**). Asterisks mark bands corresponding to predicted cleavage products. Right panels show blots for the respective gels probed for the cleavage products (**D**, **E**) or DFHO staining for Red Broccoli cleavage product (**F**). Also see Supplementary Fig. 4Bi–iii for quantification of cleavage. **G** Cleavage assays of ribozymes with varying combinations of helix 2 and helix 3 identify optimal combinations that apply across modalities (with Supplementary Fig. 4F). **H**(i) Broccoli aptamer sequence and structure. (ii) E-gene-triggered ribozyme with embedded Broccoli aptamer (T-E-gene_Cl-Broccoli). **I**(i) Cleavage assay of T-E-gene_Cl-Broccoli with increasing concentrations of trigger, stained with SYBR Gold (left) and DFHBI (right). (ii) Fraction of ribozyme dual-cleaved at increasing trigger concentration fit a hyperbolic (least squares fit) model ($R^2 = 0.96$). Data represents three biological replicates ($n = 3$) with error bars showing mean and SEM. **J** Fluorescent microplate readings of purified cleavage assays of T-E-gene_Cl-Broccoli cleaved in varying concentration of trigger allows direct readout of cleaved Broccoli as a function of trigger concentration. Data presents three biological replicates ($n = 3$) with error bars showing mean and SEM and fit a hyperbolic (least squares fit) model ($R^2 = 0.969$). Ribozyme stick cartoons are labelled and coloured according to Fig. 2B.

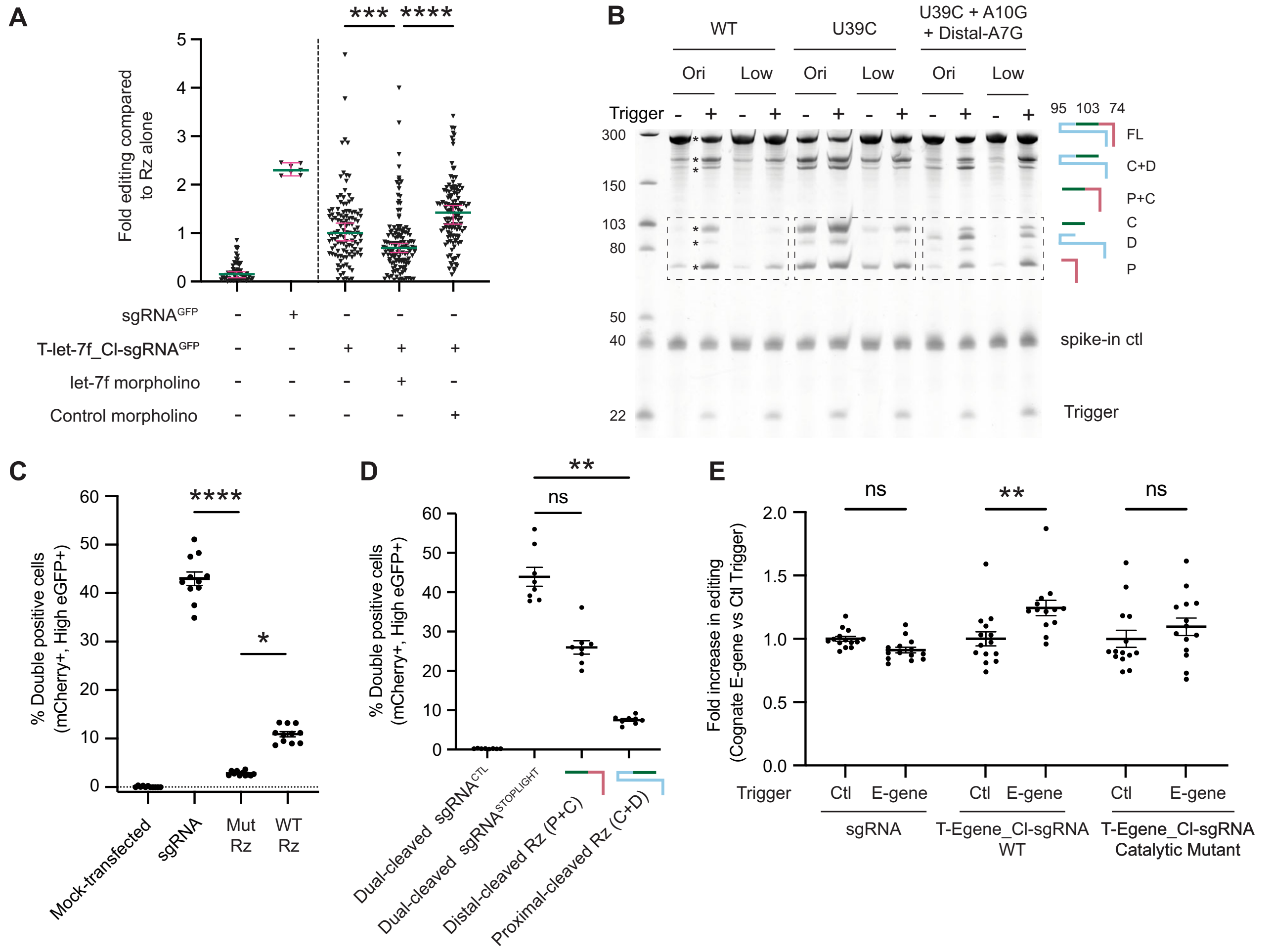

Fig. 5 | Optimised UNBAR ribozymes can cleave in a trigger-dependent manner to regulate gene expression in cellular contexts. **A** Rate of editing using DNA fragment analysis, compared to T-let-7f_Cl-sgRNA^{GFP} ribozyme alone, of uninjected ($n = 55$), positive control sgRNA^{GFP} + Cas9-injected ($n = 7$), T-let-7f_Cl-sgRNA^{GFP} ribozyme + Cas9-injected ($n = 116$), T-let-7f_Cl-sgRNA^{GFP} ribozyme + Cas9 + *let-7f* morpholino inhibitor-injected ($n = 128$) and T-let-7f_Cl-sgRNA^{GFP} ribozyme + Cas9 + control morpholino inhibitor-injected ($n = 120$) zebrafish embryos. All conditions were co-injected with Cas9 protein. Error bars: green bars label the median and magenta bars label the 95% confidence intervals. Data were pooled from three experiments, each normalised to ribozyme alone in the respective experiment. (***$p = 0.0005$, ****$p < 0.0001$). **B** Cleavage assays of wild-type, U39C and triple mutant (U39C + Dual-A10G + Distal A7G) UNBAR ribozymes in cleavage buffer with low Mg^{2+} and spermine (Low) vs. original buffer with higher Mg^{2+} and spermine levels (Ori). **C** Flow cytometry analysis of eGFP-reporter turn-on in HEK293T Stoplight^{+} spCas9^{+} reporter cells transfected with sgRNA^{STOPLIGHT} alone, or with RNA purified from cleavage assay of mutant (T-Egene_Cl-sgRNA^{STOPLIGHT}-A38CMut) or wild-type UNBAR ribozyme (T-Egene_Cl-sgRNA^{STOPLIGHT}) cleaved in low Mg^{2+}/spermine buffer (with cognate trigger)(see Supplementary Fig. 5D). (*$p = 0.044$ for Mut Rz vs WT Rz, ****$p < 0.0001$ for sgRNA vs Mut Rz; $n = 11$ for all samples). **D** Flow cytometry analysis of eGFP-reporter turn-on in HEK293T Stoplight^{+} spCas9^{+} reporter cells transfected with sgRNA^{STOPLIGHT} dual-cleaved, partially distal cleaved or proximally cleaved out of T-Egene_Cl-sgRNA^{STOPLIGHT}. (**$p = 0.0013$)($n = 8$ for all samples). **E** Flow cytometry analysis of sgRNA^{STOPLIGHT}, wildtype T-E-gene_Cl-sgRNA^{STOPLIGHT} and its A38C catalytic mutant, co-delivered in the same transfection mix with control or cognate trigger RNA (E-gene). Data were pooled from two experiments, editing rate was normalised to the editing rate of each RNA with control trigger in the respective experiment. (**$p = 0.0048$)($n = 13$–14). Ribozyme stick cartoons are labelled and coloured according to Fig. 2B. Data in (**C**–**E**) present three biological replicates with error bars showing mean and SEM. Statistical significance was assessed by non-parametric one-way ANOVA (Kruskal–Wallis) with Dunn's multiple comparisons test (**** = $p < 0.0001$, *** = $p < 0.001$, ** = $p < 0.01$, * = $p < 0.05$, ns = $p > 0.05$).

To explore this possibility, we next investigated sgRNA-embedded ribozymes in human cells. To allow for functional normalised assessment of sgRNA editing levels, we made use of HEK293T-Stoplight^{+} spCas9^{+}reporter cells (Stoplight cells), which initially express only mCherry but switch to expressing both mCherry and eGFP post-editing with sgRNA^{STOPLIGHT} but not a non-targeting sgRNA^{CTL} [60] (Supplementary Fig. 5F). We embedded sgRNA^{STOPLIGHT} within a ribozyme triggered by a fragment of the SARS-CoV-2 E-gene (T-E-gene_Cl-sgRNA^{STOPLIGHT}). This viral sequence trigger was chosen as it exhibits high specificity and signal-to-noise ratio (Figs. 2D–I and 3).

Since the concentrations of Mg^{2+} and polyamines are lower in cells (~1 mM Mg^{2+} and <0.01–0.05 mM free polyamine[61–63]) than in the buffer we used for cell-free cleavage assays in this study (7 mM Mg^{2+} and 5 mM spermine), we first assayed UNBAR cleavage in conditions of lowered Mg^{2+} and spermine. We found that cleavage of the wild-type ribozyme was substantially lower in buffer conditions that mimic cellular ionic conditions (Fig. 5B). It was previously reported that mutations A$_{7}$G, A$_{10}$G and U$_{39}$C can improve HpRz cleavage[64,65]. Hence, we tested these variants singly or in combination. We found that UNBAR ribozymes with either U39C alone or all three mutations combined showed trigger-dependent cleavage rates in cellular ionic conditions that were comparable to that in the original cell-free cleavage buffer, whilst keeping trigger-independent background cleavage low (Fig. 5B).

We incorporated a U39C mutation into a T-E-gene_Cl-sgRNA^{STOPLIGHT} ribozyme to study its cleavage and function in human cells. This ribozyme exhibited robust trigger-dependent cleavage in cell-free assays (Supplementary Fig. 5Gi) only with cognate and not control trigger (Supplementary Fig. 5Gii, iii; $p < 0.05$), and its corresponding A38C catalytic mutant did not cleave (Supplementary Fig. 5Gii). Using this ribozyme, we systematically investigated: (1) Effect of ribozyme cleavage scars on sgRNA efficacy; (2) Whether embedding the sgRNA within a ribozyme scaffold was sufficient to block sgRNA function; (3) The maximal functional turn-on signal in human cells if cleavage occurs at rates similar to cell-free assays, (4) Efficacy of partially cleaved UNBAR fragments on gene editing; (5) Whether we can visualise trigger-dependent cleavage product release in cells; and (6) Whether trigger-induced cleavage of ribozymes in cells can produce a switch in functional CRISPR-Cas9 editing output.

Ribozyme cleavage occurs at specific sequences (Fig. 1A). In the case of UNBAR, the cleavage product retains 5′-GUC and 3′-CA scars. While guide RNAs beginning with a GUC would be able to cleave within UNBAR without additional sequences, in the case of sgRNA^{STOPLIGHT}, a 5′ GUC was appended to enable cleavage. To investigate the effect of cleavage scars on the functional activity of sgRNA^{STOPLIGHT} released from UNBAR, we measured editing by sgRNA^{STOPLIGHT} with no cleavage scars, compared to the same sgRNA with 5′, 3′ or both 5′ and 3′ cleavage scars, as well as a non-targeting control sgRNA (sgRNA^{CTL}; Supplementary Fig. 5H)[60] with cleavage scars. An sgRNA with a 3′ cleavage scar edited as efficiently as the sgRNA with no scar (>70% double-positive cells; $p > 0.05$), while sgRNAs with a 5′ or both 5′ and 3′ cleavage scars exhibited reduced editing (~40% double-positive cells; $p \sim 0.05$ or $p < 0.01$, respectively). The non-targeting sgRNA^{CTL} did not edit (Supplementary Fig. 5H). Nonetheless, a ~ 40% editing activity of sgRNA with both a 5′ and 3′ cleavage scar, still provided a sufficient dynamic range to study regulation of gene editing by UNBAR ribozymes.

Next, we asked whether the ribozyme was able to sequester embedded sgRNA within its scaffold to prevent its editing activity. Embedding sgRNA^{STOPLIGHT} within a mutant ribozyme reduced editing in mammalian cells (~2.8% double-positive cells) compared to the sgRNA alone (~43.0% double-positive cells) (Fig. 5C; $p < 0.0001$), which is a ~ 15-fold repression of eGFP turn-on by the sgRNA when it was embedded within the ribozyme compared to free sgRNA. Therefore, embedding the sgRNA within the ribozyme efficiently blocks its editing efficacy in mammalian cells. We then investigated the maximal eGFP turn-on that could be achieved by trigger-activated sgRNA released from UNBAR ribozyme, if ribozyme cleavage occurred to the same extent in the cell as was observed in cell-free cleavage assays. To test this, we purified and transfected RNA of mutant and wild-type UNBAR ribozymes pre-cleaved in low Mg^{2+}/ spermine buffer (Supplementary Fig. 5I) into Stoplight cells. Flow cytometry analyses showed a significant ~4-fold increase in eGFP levels induced by wild-type cleaved UNBAR ribozyme (~10.9% double-positive cells) compared to its catalytic mutant (~2.8%; $p = 0.044$, Fig. 5C).

To investigate the effects of partially cleaved T-E-gene_Cl-sgRNA^{STOPLIGHT} on gene editing, we transcribed RNA fragments that mimic partial cleavage at either the distal or proximal cleavage site. SgRNA corresponding to dual-cleaved UNBAR (with cleavage scars) exhibited the highest editing efficiency (~40%), non-significantly higher than partially distal-cleaved fragment (P + C; with a 5′ overhang), which also robustly activated gene editing (~25%), while partially proximal-cleaved fragment (C + D; with a 3′ overhang) had a much lower editing efficacy (~6%; $p < 0.01$)(Fig. 5D).Therefore, partially cleaved T-E-gene_Cl-sgRNA^{STOPLIGHT} ribozymes can also contribute to gene editing signal.

Next, to visualise trigger-dependent cleavage within cells, we co-transfected T-E-gene_Cl-sgRNA^{STOPLIGHT} ribozyme with control or cognate E-gene trigger. We observed only a small amount of dual-cleaved product released in HEK293T cells (Supplementary Fig. 5J; lanes 4–9). Northern blotting of the transfection mix sample at 24 h showed no ribozyme cleavage (Supplementary Fig. 5J; lanes 1, 2). Hypothesising that spermine[66], a naturally occurring polyamine[67], may aid cleavage, we asked whether supplying spermine to cells would improve ribozyme cleavage within cells. This approach also allowed us to definitively test whether cleavage could occur within cells.

HEK293T cells were transfected with T-E-gene_Cl-sgRNA^{STOPLIGHT} ribozyme and either control or cognate trigger. After 24 h, all media and transfection mix were removed from the culture wells, so that any ribozyme remaining must have entered cells to be protected from the media removal. At this point, we incubated the cells with either normal or spermine-supplemented replacement media. Ribozymes from cells replaced with normal media exhibited limited cleavage by 72 h (Supplementary Fig. 5J, lane 9). In contrast, ribozymes from cells replaced with spermine-supplemented media exhibited robust cleavage, with a marked increase in cleavage product released just 2 h after spermine addition, at 26 h (lane 11), with a further increase at the 48 h mark (lane 13). Notably, RNA in the transfection mix alone at 24 h (lane 2) did not show detectable cleavage product, in contrast to RNA from spermine-treated cells tested just 2 h later (lane 11). These results demonstrate that substantial ribozyme cleavage occurred in cells after media with transfection mix was removed at 24 h, only with cognate trigger and not control trigger.

Since cleavage can be observed in HEK293T supplemented with spermine, this allowed us to test ribozyme cleavage and function in HEK293T-Stoplight+ spCas9+ reporter cells with certainty that cleavage could only have occurred post-spermine incubation, within cells. We examined editing by sgRNA^{STOPLIGHT}, wild-type T-E-gene_Cl-sgRNA^{STOPLIGHT} and its corresponding catalytic mutant ribozyme co-transfected with control or cognate E-gene trigger into Stoplight cells using flow cytometry. While E-gene co-transfection had no effect on editing by sgRNA^{STOPLIGHT} alone or mutant ribozyme ($p > 0.05$), its co-transfection with wildtype T-E-gene_Cl-sgRNA^{STOPLIGHT} ribozyme caused ~24% increase in editing rates compared to those incubated with control trigger ($p < 0.01$) (Fig. 5E). As an additional control, we examined the effect of co-incubation of control vs. cognate E-gene trigger on wild-type and mutant ribozymes that comprise a non-targeting sgRNA^{CTL} [60], and observed no editing (Supplementary Fig. 5K). Therefore, ribozymes can cleave in a trigger-dependent manner in human cells to regulate gene editing.

In summary, northern blotting and functional data provide evidence for trigger-dependent cleavage and CRISPR-Cas9 gene editing by UNBAR ribozymes in cellular contexts. With further engineering, UNBAR ribozymes have the potential to be developed for RNA sensing-dependent functions of embedded ncRNA effectors for regulation of gene expression.

Discussion

In this study, we describe the development of an innovative signal-transducing RNA modality: a programmable self-cleaving ribozyme that exhibits RNA trigger-dependent cleavage and release of a ncRNA embedded between dual cleavage sites. To our knowledge, UNBAR is the first example of a true dual-site-cleaving single ribozyme within which almost any short RNA cleavage product can be embedded. The cleavage product and RNA-sensing regions of UNBAR are separate, with no sequence interdependence, and can therefore be modularly designed. UNBAR ribozymes can transduce and amplify RNA signals in a protein-free and template-free manner by RNA catalysis, without alteration of the original trigger.

Amplification may occur at least partly through trans-cleavage (Fig. 2J), a unique property of ribozymes. Due to the ribozymes' trans-cleaving characteristics, they cannot be multiplexed to differentiate between different triggers to release different cleavage products, including within the same cellular system. The entire system is compactly encoded in one ~200–300-nt strand of RNA, without the need for protein or DNA co-factors. For cellular applications, this may avoid undesired adaptive immune responses to extraneous foreign proteins (although exogenous RNA and some delivery systems can still activate innate immune sensing) and dependence on varying host-cell protein expression machinery. Therefore, UNBAR ribozymes are a broadly generalisable and modular platform for detection, conversion and amplification of one RNA signal into another, with almost no sequence constraints.

We designed ribozymes that can detect and bind miRNA and viral sequences, upon which they cleave to release various types of ncRNA, including short RNA, sgRNA, shRNA and aptamer. Broccoli-releasing ribozymes carry out one-step direct detection, amplification and transduction of RNA trigger to a functional (fluorescent) readout (Fig. 4I, J). We optimised multiple ribozyme regions to achieve high signal-to-noise ratio of cleavage product release in the presence vs. absence of trigger, resulting in UNBAR ribozymes that can distinguish between similar target sequences at up to single-nucleotide sensitivity (Fig. 2H). Computational modelling of an E-gene-triggered ribozyme identified an auto-inhibitory effect by unbound trigger arms, which results in low leakiness and a large turn-on signal for this ribozyme. The models we created accurately reproduce the behaviour observed experimentally, particularly the sensitivity of signal-to-noise ratio on H4 stability. Computational and structural analyses can help us to understand why some triggers and designs perform better. These studies show that UNBAR is modular in concept, but careful sequence-aware design is necessary for maximal performance. Engineering strategies described in this study can be explored to optimise trigger-dependency for a specific trigger sequence.

We found that compensatory mechanisms can render some essential nucleotides mutable (Supplementary Fig. 4A); these expand the repertoire of sequences that can be encoded with minimal cleavage 'scars'. We also identified variants that can cleave in cellular ionic conditions (Fig. 5B) and demonstrated that optimised ribozymes can cleave in a trigger-dependent manner in human cells (Supplementary Fig. 5J). UNBAR cleavage in some cell types may benefit from supplementation of spermine, a naturally occurring polyamine found in many foods[67]; understanding the underlying mechanism will enable further engineering for improved future iterations of UNBAR. Higher-throughput methods like massively parallel sequencing[68] and directed evolution using cellular readouts would allow exploration of large sequence spaces to potentially discover ribozymes with improved function.

We observed that optimised UNBAR ribozymes can regulate gene editing in cellular contexts in a cleavage-dependent and trigger-dependent manner; co-transfection of a viral RNA trigger significantly increased cellular editing by ~23% compared to the control trigger (Fig. 5E). However, the impact of cleavage scars and partially cleaved fragments will impact efficacy and selection of UNBAR cleavage product design and applications. In the case of cleavage scars, it would be preferred to screen for cleavage products that function efficiently with 5′GUC and 3′-CA cleavage scar overhangs. For partial cleavage, while in the case of the Broccoli-releasing ribozyme, only the dual-cleaved product exhibited fluorescence (Fig. 4I, J); however, for sgRNAs, partial cleavage products were able to activate gene editing (Fig. 5D). Nonetheless, by pairing the flow cytometry results with northern blot analysis, we can confidently attribute gene-editing activity to the specific combination of cleaved UNBAR fragments present. Therefore, partial cleavage must be considered and tested for each modality. In addition, sgRNA-embedded UNBAR does not currently attain the gene editing levels observed with direct sgRNA delivery (Fig. 5C), likely due to incomplete cleavage. Engineering of UNBAR to optimise robust trigger-dependent dual-site cleavage will be required to improve UNBAR function on these fronts.

Importantly, many ribozyme modalities are developed to be expressed from plasmids[28–30,69], as ribozymes usually autocleave if delivered as RNA. In contrast, UNBAR ribozymes can be delivered into cells as RNA prior to cleavage, and triggered to cleave in the cell, as a result of this novel advance of trigger-activated ribozymes that do not auto-cleave during in vitro transcription. However, pre-cleaved ribozymes showed only a four-fold increase in editing compared to uncleaved mutant ribozymes (Fig. 5C). This suggests that further improvements to delivery, stability, and cleavage in cells remain to be explored. In addition whether which species and the sensitivity with which UNBAR can detect endogenous RNAs in the cell are interesting questions to be followed up upon in future studies. UNBAR ribozyme could also potentially be genetically encoded in a transgene to enable a further range of applications; however, we observed that the expression levels of a catalytically inactive UNBAR were ~5-fold lower than the cleavage product (CsgRNA) alone when either was expressed under a U6 promoter (Supplementary Fig. 5L). Hence, UNBAR integrity, trigger-dependent cleavage and cleavage-dependent function remain to be studied and optimised when expressed from a transgene.

In summary, this study introduces a novel ribozyme-based platform for RNA signal transduction and demonstrates that it can function in cellular contexts when the trigger is bound. It can be further explored for a range of potential applications in synthetic biology, disease diagnostics and gene regulation.

Methods

Ethical statement

Our research complies with all relevant ethical regulations. Our study protocols were approved by the Institutional Biosafety Committee at Institute of Molecular and Cell Biology, A*STAR, Singapore. All experiments with zebrafish embryos were approved by the Singapore National Advisory Committee on Laboratory Animal Research (Protocol number: 221702).

PCR amplification of the template and in vitro transcription of RNA

DNA templates and primers were ordered from Integrated DNA Technologies, USA, and PCR amplification was performed using Phusion High-Fidelity PCR Master mix (#F531L, Thermo Fisher Scientific, USA) according to the manufacturer's instructions. PCR products were purified using QIAquick PCR Purification kit (#28106, Qiagen, Germany), or gel-extracted using Zymoclean Gel DNA Recovery Kit (ZYR.D4008, Zymo Research, USA), and used as templates for in vitro transcription using AmpliScribe T7-Flash transcription kit (#LGLC-ASF3507, Lucigen, USA) according to the manufacturer's instructions. For some templates, DNA gene fragments, oligo pools or clonal genes (Twist Bioscience, USA) were used for in vitro transcription. GGGA would be added to the 5′ end of every transcript during T7 transcription. After the in vitro transcription reaction and DNaseI treatment as per manufacturer's instructions, 280 µL of RNase-free water (#SH30538.02, HyClone, USA) was added to 20 µL of the in vitro transcription reaction. The RNA was purified by adding 300 µL of acid-phenol:chloroform, pH 4.5 (with IAA, 125:24:1) (#AM9722, Invitrogen, USA), mixed, and centrifuged at 18,000 × *g* for 3 min at room temperature. The aqueous phase was transferred to a new tube, and 300 µL of chloroform (#07278-00, Kanto Chemical, Japan) was added. The mixture was centrifuged at 18,000 × *g* for 3 min at room temperature. The aqueous phase was transferred to a new tube and the RNA was precipitated with 1/10 volume (25 µL) of 3 M sodium acetate (pH 5.2) and 2.5× volume (625 µL) of absolute ethanol. After overnight precipitation at −20 °C, the samples were centrifuged at 16,000 × *g* for 20 min at 4 °C. The supernatant was discarded and the RNA pellet was washed with cold 75% ethanol and centrifuged at 16,000 × g for 20 min at 4 °C. After centrifugation, the supernatant was removed completely, and the pellet was allowed to air-dry. The RNA was then resuspended in

50 µL of RNase-free water, and its concentration was measured using a NanoDrop spectrophotometer (Thermo Fisher Scientific).

Cell-free cleavage assays

Assays were performed with in vitro transcribed ribozyme RNA (200 nM unless otherwise described) and trigger RNA (50 nM unless otherwise described) (Integrated DNA Technologies, USA) in 1× cleavage buffer. For tandem ribozyme cleavage assays: composition of the cleavage buffer used is 50 mM Tris, 12 mM MgCl2, 5 mM Spermine, pH 7.4. Reaction conditions were as follows: 60 °C for 1 min, 56.5 °C for 1 min, 53 °C for 1 min, 49.5 °C for 1 min, 46 °C for 1 min, 42.5 °C for 1 min, 39 °C for 1 min, 37 °C, 15 mins; Steps 1 to 8 were repeated for 9 cycles.

For single ribozyme cleavage assays: cleavage buffer contained (10 mM Tris, 7 mM magnesium chloride, 5 mM spermine, 2 mM sodium chloride, pH 6.4). For conditions with lowered Mg^{2+} and spermine, 1× cleavage buffer comprised pH 6.4 with 10 mM Tris, 1 mM magnesium chloride, 0.05 mM spermine, and 2 mM sodium chloride. 200 nM of an inert 40-nt RNA sequence (5′-GGGACAUGGAAGUCACACCUUC GGGAACGUGGUUGACCUA-3′) was spiked into the reaction as a loading control in the cleavage assay master mix. Reactions were incubated at 37 °C for 4 h.

Detection and visualisation of cleavage product

Cleavage reaction product was directly mixed with 2× RNA Loading Dye (#B0363S, New England Biolabs, USA), then heat-denatured at 70 °C for 10 min and separated on a 10% denaturing polyacrylamide gel (#EC-833, National Diagnostics, USA) in 1× TBE (Tris/Boric Acid/EDTA) buffer (#1610770, Bio-Rad, USA) at 200 V for 45 min to 1 h, or until the dye front migrated to the bottom of the gel. Low range ssRNA ladder (#N0364S, New England Biolabs) was loaded as a size marker, and 25 ng of an RNA oligonucleotide, e.g. 29-nt oligo (5′-GUCCUUA-GUCGAAAGUUUUACUAGAGUCA-3′) (Integrated DNA Technologies), or an in vitro transcribed RNA sequence corresponding to the size of the expected cleavage product, was spiked into the ladder as an additional size marker. Where appropriate, 25 ng each of the in vitro-transcribed ribozyme, trigger and/or spike-in sequence were also added into the ladder as size markers. Gels were stained with SYBR Gold at 1:10,000 dilution (#S11494, Invitrogen), and were visualised using a ChemiDoc MP Imaging System and analysed with Image Lab software (Bio-Rad), or using an iBright FL1500 and analysed with iBright Analysis software (Thermo Fisher Scientific).

Densitometry analyses and calculation of fraction dual-cleaved

Gel images stained with SYBR gold were analysed using the Image Lab software. The adjusted volume intensity was measured for the full-length band, the partially cleaved fragments (C + D, P + C), and the dual cleaved product (C). To account for fragment size, each measured intensity was normalised to the corresponding fragment length. The fraction of ribozyme dual-cleaved was then calculated as the ratio of the normalised intensity of the dual-cleaved fragment to the total normalised intensity of all fragments (full length (FL), the partially cleaved fragments (C + D, P + C), and the dual-cleaved fragment (C)).

Northern blotting

RNA was transferred onto a Hybond-N+ membrane (#RPN303B, GE Healthcare, USA) using the Transblot SD semi-dry transfer cell (Bio-Rad), in 1× TBE at 10 V and 300 mA for 1 h at 4 °C. The membrane was cross-linked using a UV crosslinker (Analytik Jena, USA), and pre-hybridised in PerfectHyb Plus Hybridisation Buffer (#H7033-1L, Merck, USA) at 45 °C for 5 min with rotation in a hybridisation oven. 5′ Alexa Fluor 647- or Cy5-labelled DNA probe (Integrated DNA Technologies, see Sequence Listing in Supplementary Data 1) against the cleavage product was added to the pre-hybridisation solution and further incubated at 45 °C for 3 h with rotation. Following hybridisation, membranes were washed progressively with increasing stringency of wash buffer (low stringency: 2X SSC, 0.1% SDS; high stringency: 0.5X SSC, 0.1% SDS; ultra-high stringency: 0.1X SSC, 0.1% SDS). All washing steps were performed at 45 °C in a hybridisation oven with 20 min rotation (except for low stringency wash, which was performed at room temperature with 5 min rotation). Membranes were visualised using a ChemiDoc MP Imaging System and analysed with Image Lab software (Bio-Rad), or using an iBright FL1500 and analysed with iBright Analysis software (Thermo Fisher Scientific).

Broccoli sensor experiments

Cloning and digest of template plasmid for IVT. The DNA gene fragment (Twist Bioscience) containing the T7 promoter sequence followed by the ribozyme sequence for T-E-gene_Cl-Broccoli was amplified with the Phusion High Fidelity PCR Master Mix with HF Buffer (#F531L, Thermo Fisher Scientific) using primers SK63 (5′-TAAGCATCTAGACACCTGCCGGATGAAGTATAATACGACTCACTATA GGGA-3′) and SK64 (5′-TGCTTAACCGGTCACCTGCTCCGTTCGGAAG AGTCGTGTTT-3′) to include XbaI_PaqCI and PaqCI_BshTI sites on each DNA end, respectively (Integrated DNA Technologies). The PCR product was purified with the FavorPrep™ GEL/PCR Purification Kit (#FAGCK 001-1, Favorgen, Taiwan) according to the manufacturer's protocol. The amplicon and the plasmid backbone, pcDNA3.3_eGFP (Addgene plasmid #26822[70]; http://n2t.net/addgene:26822; RRID:Addgene_26822), were digested with FD XbaI and FD BshTI (#FD0684 and #FD1464, Thermo Fisher Scientific) before being gel-isolated with the FavorPrep™ GEL/PCR Purification Kit. Digested backbone and insert were ligated with T4 DNA Ligase (#M0202L, New England Biolabs) and transformed to One Shot TOP10 Chemically Competent cells (#C404006, Invitrogen). Plasmids from positive transformants were prepared with a QIAprep Spin Miniprep Kit (#27106, Qiagen) and verified with Sanger sequencing (Bio Basic Asia Pacific, Singapore). To obtain the linearised DNA template for IVT, the sequence-verified plasmid was digested with PaqCI (#R0745L, New England Biolabs, USA) and gel-isolated with the FavorPrep™ GEL/PCR Purification Kit.

Ribozyme cleavage reaction and DFHBI-1T-based fluorescence reading

T-E-gene_Cl-Broccoli ribozyme was synthesised through in vitro transcription using AmpliScribe T7-Flash transcription kit with either plasmid-derived linearised DNA template or DNA gene fragment (Twist Bioscience) before purification with a Monarch® Spin RNA Cleanup Kit (#T2040L, New England Biolabs). Cell-free cleavage assays were performed with 1 or 2.5 µM of ribozyme RNA and varying amount of trigger RNA (5′-UUCGGAAGAGACAGGUACGU-3′; Integrated DNA Technologies) in 1× cleavage buffer (10 mM Tris, 7 mM $MgCl_2$, 5 mM spermine, 2 mM sodium chloride, pH 7.0). To this end, IVT RNA prepared using DNA gene fragment was used for this experiment with 2.5 µM ribozyme, and IVT RNA prepared using template from digested plasmid was used for experiments with 1 µM ribozyme. The reaction was incubated at 37 °C for 4 h, and the cleavage product was then purified with the Monarch® Spin RNA Cleanup Kit and eluted in 20 µL of RNase-free water.

For DFHBI-1T-based fluorescence reading, 16.25 µL of either RNase-free water or purified cleavage product was mixed to obtain a final reading solution with 10 µM DFHBI-1T (unless otherwise stated; Lucerna Technologies, USA), 40 mM HEPES pH 7.4, 125 mM KCl and 1 mM $MgCl_2$. Reactions were loaded into a 384-well polypropylene F-bottom plate (#781209, Greiner Bio-One, Germany) and incubated at 37 °C for 1 h. Fluorescence signal was recorded using a BioTek Synergy Neo 2 fluorescence microplate reader (Agilent, USA) with excitation wavelength 460/10 nm, emission wavelength 501/10 nm, and extended dynamic range. Experiments were carried out in duplicate for each data point, and fluorescence fold change was reported as the ratio between absolute fluorescence signal from the sample over the mean of absolute fluorescence signal from the no-trigger cleavage product.

In-gel DFHBI-1T staining

After RNA samples were separated on a 10% denaturing polyacrylamide gel, the gels were washed in RNase-free water thrice for 5 min each. Gels were subsequently soaked with a staining buffer containing 10 μM DFHBI-1T, 40 mM HEPES pH 7.4, 100 mM KCl and 1 mM $MgCl_2$ in the dark for 30 min. Gels were then visualised using a ChemiDoc Imaging System under the AF488 channel. Before a subsequent SYBR Gold staining, gels were washed in RNase-free water thrice for 5 min each.

Zebrafish micro-injection and genomic extraction

Wild-type, heterozygous and homozygous *foxj1b:GFP* (T2BGSZ10 Gt(foxj1b:GFP))[59] transgenic zebrafish were maintained under standard conditions of fish husbandry. All experiments with zebrafish embryos were approved by the Singapore National Advisory Committee on Laboratory Animal Research (Protocol number: 221702).

Ribozyme RNA for injection into fish was in vitro transcribed from T7 promoter-driven DNA templates using MEGAscript T7 Transciption Kit (#AM1334, Thermo Fisher Scientific, USA). Ribonucleoprotein mixture (RNP) containing 300 ng/μL of in vitro transcribed ribozyme RNA and 0.5 μg/μL of Cas9 protein (#TGEN_CP2, ToolGen/nSAGE Inc., South Korea) was incubated at 37 °C for 10 min and allowed to cool to room temperature. Each embryo was injected with 0.75 nL of RNP mixture (~0.22 ng or 2.5 fmol of ribozyme per embryo). hsa-let-7f (mA/ZEN/mA mCmUmA mUmAmC mAmAmU mCmUmA mCmUmA mCmCmU mC/3ZEN/) or negative control (NC1) morpholino (Integrated DNA Technologies) were introduced into the RNP mix at a final concentration of 8 μM.

Genomic DNA was extracted from healthy single embryos 24 h after micro-injection. Each embryo was first rinsed with 1× PBS (#10010023, Gibco, USA), followed by addition of 20 μL alkaline lysis solution (25 mM sodium hydroxide, 0.2 mM EDTA) and incubation at 95 °C for 30 min. The tubes were vortexed to check for complete lysis of embryos and then incubated at 95 °C for another 10 min. Twenty microliters of neutralisation buffer (40 mM Tris-HCl, pH 8.0) was added to each tube.

miRNA inhibitor

hsa-*let-7*f inhibitor (mA/ZEN/mA mCmUmA mUmAmC mAmAmU mCmUmA mCmUmA mCmCmU mC/3ZEN/) and control inhibitor NC1 (mG/ZEN/mC mGmUmA mUmUmA mUmAmG mCmCmG mAmUmU mAmAmC mG/3ZEN) were purchased from Integrated DNA Technologies.

DNA fragment analysis of genome editing

Two microliters of extracted genomic DNA from fish was used as the template for PCR amplification of GFP using primers SAW907_GFPF2 (5′-GTGGTGCCCATCCTGGTC-3′) and SAW908_GFPR2 (5′-CTTGTACAGCTCGTCCATGC-3′). The GFP band was gel-isolated (Zymoclean Gel DNA Recovery kit #D4002, Zymo Research, USA) and used as the template for a second PCR using fluorophore-labelled primers (FW + M13 adaptor (5′-TGTAAAACGACGGCCAGTACGTAAACGGCCACAAGT-3′) and RV (5′-TGAAGAAGATGGTGCGCTC-3′)). Capillary electrophoresis was run on an ABI 3730xl DNA Analyzer (Applied Biosystems, USA). The fluorescently labelled DNA fragments were sized by comparison to a size standard (#4322682, Applied Biosystems). Data analysis was performed using GeneMapper (Applied Biosystems).

Maintenance of cell cultures

HEK293T (cell line received from Yan Chuan's lab, IMCB) and HEK293 Stoplight$^+$ SpCas9$^+$ (cell line received from Pieter Vader's lab, University Medical Center Utrecht) cells[60] were cultured in Dulbecco's modified Eagle's medium (DMEM/High Glucose) with L-glutamine (#SH30022.01, HyClone) supplemented with 10% heat-inactivated foetal bovine serum (#10270106, Gibco) and 1% penicillin/streptomycin (#15140122, Gibco). For the HEK293 Stoplight+ SpCas9+ cells, the medium was further supplemented with 1000 μg/mL G418 (#10131027, Thermo Fisher Scientific) and 5 μg/mL Blasticidin S HCl (#A1113903, Thermo Fisher Scientific).

Transfection of ribozymes

For Fig. Fig. 5C, RNAs were first synthesized through in vitro transcription using AmpliScribe T7-Flash transcription kit with DNA gene fragment (Twist Bioscience) before purification with Monarch® Spin RNA Cleanup Kit (#T2040L, New England Biolabs). Cell-free cleavage assays were performed in 1x cleavage buffer (10 mM Tris, 7 mM MgCl2, 5 mM spermine, 2 mM sodium chloride, pH 7.0). The reaction was incubated at 37 °C for 4 h, and the cleavage product was then purified with the Monarch® Spin RNA Cleanup Kit and eluted in 30 μL of RNase-free water. HEK293T Stoplight+ SpCas9+ cells were seeded at a density of 2×10^4 cells per well in a 96-well culture plate. After 24 h post-seeding, 3 pmol equivalent amount of ribozyme RNA was transfected using 3 μL of LipofectamineTM RNAiMAX Transfection Reagent (#13778150, Invitrogen) in Opti-MEMTM I Reduced Serum Medium (#31985070, Gibco) following the manufacturer's protocol. After 48 h post-transfection, cells were collected and prepared for flow analysis. For Fig. Fig. 5D, HEK293T Stoplight+ SpCas9+ cells were similarly seeded and after 24 h post-seeding, 3 pmol of ribozyme RNA and 3 pmol of trigger RNA were transfected using 3 μL of Lipofectamine™ RNAiMAX Transfection Reagent in Opti-MEM™ I Reduced Serum Medium following the manufacturer's protocol. After 24 h post-transfection, the medium was removed, and replaced with HEK293 Stoplight+ SpCas9+ maintenance culture media without foetal bovine serum (#10270106, Gibco), but with spermine supplementation at 800uM. After 48 h of spermine treatment, cells were collected and prepared for flow analysis.

For Supplementary Fig. 5J, HEK293T cells were seeded at a density of 1×10^5 cells per well in 12-well culture plate. After 24 h, 30 pmol of ribozyme RNA and 30 pmol of the trigger RNA were transfected using 3 μL of Lipofectamine™ RNAiMAX Transfection Reagent (#13778150, Invitrogen) in Opti-MEM™ I Reduced Serum Medium (#31985070, Gibco) following the manufacturer's protocol. At 24 h post-transfection, the medium was replaced with fresh medium either without or with 800uM spermine supplementation. Cells without spermine were harvested at 24 h, 48 h and 72 h post-transfection, whereas spermine-treated cells were collected at 2 h, 24 h and 48 h after spermine addition. Total RNA was extracted using Trizol (#15596018, Invitrogen) according to the manufacturer's protocol. To detect ribozyme cleavage in the cells, 10 μg of the extracted total RNA was loaded onto a 10% denaturing gel, and as a control, 8 μl of the 24-h transfection mix only sample was also loaded and northern blotting was performed using a sequence-specific fluorescent probe.

For Supplementary Fig. 5L, the sgRNA-embedded catalytic mutant UNBAR and the sgRNA cleavage product (CsgRNA) were cloned under the pLKO.1 puro construct driven by U6 promoter (Addgene plasmid # 8453; http://n2t.net/addgene:8453; RRID:Addgene_8453)[71] and transfected into HEK293T cells using Lipofectamine 3000 (#L3000015, Invitrogen). 1.5×10^5 cells per well were seeded into a 12-well culture plate. After 24 h, 1 μg of plasmid expressing UNBAR was transfected along with 30 pmol of specific trigger RNA /52MOErT/i2MOErG/i2MOErA/rGrGrUrArGrUrArGrArUrUrGrUrArUrA/i2MOErG/i2MOErT/32MOErT/ (Integrated DNA Technologies, USA). 1 μg of U6-driven CsgRNA was also transfected.. Forty-eight hours post-transfection, total RNA was isolated using Trizol (#15596018, Invitrogen) according to the manufacturer's protocol. Twelve micrograms of the extracted total RNA was loaded onto each lane in the 10% denaturing gel and northern blotting was done using specific fluorescent probe.

Flow cytometry

Cells in 96-well plates were dislodged from the well with 0.05% Trypsin-EDTA (1X), phenol red (#25300054, Gibco) and neutralised with complete media. The entire volume from each well was transferred to a U-bottom 96-well plate. The plate was spun down at 300 × *g* for 4 min at 4 °C, and the supernatant was discarded. Cells were stained with LIVE/DEAD Fixable Dead Cell Stain (Blue, Invitrogen, L34961 was used for HEK293T Stoplight$^+$ spCas9$^+$ cells) diluted at 1:1000 in 1× PBS (#10010023, Gibco, USA) for 15 min at room temperature. After staining, the plate was spun down at 300 × *g* for 4 min at 4 °C, and the supernatant was discarded. Cells were re-suspended in 100 µL 1× PBS (#10010023, Gibco) per well and analysed on a BD FACSymphony™ A5 flow cytometer. A figure exemplifying the gating strategy is provided in Supplementary Fig. 6. Briefly, cell debris was first gated out, and cells were selected using SSC and FSC. Then, single cells were selected by plotting FSC-A vs. FSC-H. Cells were stained with LIVE/DEAD Fixable Dead Cell Stain (Blue, Invitrogen, L34961) for HEK293T Stoplight+ spCas9+ cells. Therefore, viable cells were selected by plotting FSC-A vs. UV9-A plot for (high signal excluded). For HEK293T Stoplight+ spCas9+ cells, mCherry signal was selected using the yellow-green laser (561 nm) and eGFP signal was similarly assessed using blue laser (488 nm). The same gates were used for all samples and conditions within the same experiment. Data analysis was carried out using FlowJo (BD Biosciences, USA).

Confocal imaging

Transfected Stoplight cells were fixed with 4% paraformaldehyde (#15710, Electron Microscopy Sciences, USA) in 1× PBS (#20012-027, Gibco, USA) for 10 min at room temperature and rinsed twice with 1× PBS (#20012-027, Gibco, USA). Following fixation, cells were stained with DAPI (#62248, Thermo Scientific, USA) 1:1000 in 1× PBS (#20012-027, Gibco, USA) for 10 min at room temperature, rinsed with 1× PBS and then mounted in VECTASHIELD (H-1000, Vector Laboratories, USA). Confocal images were acquired using Olympus FV3000RS Upright confocal microscope with a 20× objective. Image annotations were performed using ImageJ.

Data, statistics and reproducibility

All experiments in the main figures were carried out at least twice, with consistent results. Statistical analyses were carried out using Graphpad Prism (GraphPad Software, Inc., CA, US).

For experiments where data from multiple experiments were pooled, the rate of editing was normalised to the control. For Fig. 5E, the editing rate for the cognate trigger + sgRNA or ribozyme sample was normalised to that for the respective control trigger. The experiment was carried out twice and the normalised data from the two experiments were pooled. For the fish experiment (Fig. 5A), the editing rate for each sample was normalised to the median of the ribozyme-only-injected sample for each experiment. The experiment was carried out three times, and the normalised data from the three experiments were pooled.

For statistical analyses with two samples, a non-parametric Mann–Whitney test was used. For experiments with 3 or more samples, non-parametric one-way ANOVA with Dunn's multiple comparisons test post hoc test was used to determine which were statistically significant outcomes. For the determination of the fraction dual-cleaved, a Friedman test was used to match bands from the same gel. For all others, a Kruskal–Wallis test was used.

Uncropped and unprocessed scans are compiled in the Source data file.

Molecular modelling

Secondary structure prediction and structure ensemble generation. RNA folding experiments were conducted with RNAstructure (version 6.4)[72]. Pairing probabilities were calculated from a given UNBAR ribozyme sequence during the initial analysis step. This was achieved by running *partition-smp* on T-SARS-CoV-2 E-gene_Cl-29nt-clvRNA UNBAR ribozyme constructs with varying H2 or H4 sequences in both + and -trigger-bound states. Calculated pairing probabilities were then used to sample 1000 structures from the Boltzmann ensemble with *stochastic-smp*. Folding free energy changes for each structure within the representative ensemble were calculated with *efn2-smp*. MFE structures for a given UNBAR construct were calculated using *Fold-smp* with the *-mfe* flag on.

Scaling, secondary structure clustering and centroid structure determination. Scaling and clustering procedures used in this study were adapted from Ding et al.[73]. Prior to distance calculations and dimensionality reduction, duplicate structures were removed from the ensemble such that N unique structures comprise a separate 'filtered' ensemble. Any unique secondary structure I of a given UNBAR ribozyme of length n can be expressed as an $n \times n$ matrix of binary base-pairing indicators $\left\{I_{ij}\right\}$ where $I_{ij} = 1$ if the ith and jth base are paired and $I_{ij} = 0$ if the ith location is single stranded. Differences between all secondary structure pairs were used to construct an $N \times N$ pairwise distance matrix. The distance between any two pairs of structures can be defined by distance metric D: $D(I_1, I_2) = \sum 1 \le i < j \le n \left|I_{ij}^1 - I_{ij}^2\right|$ where $I_1 = \left\{I_{ij}^1\right\}$ and $I_2 = \left\{I_{ij}^2\right\}$. Multidimensional scaling was then performed on the resulting distance matrix using the *scikit-learn* package (version 1.2.0) to yield the coordinates of two-dimensional embeddings required for clustering analysis and plotting.

K-Means was selected for clustering analyses after comparing the performance of all available algorithms in the *scikit-learn.cluster* module. To determine the optimal number of clusters for a given set of embedded coordinates, K-Means was run iteratively over a range of 2–20 such that for each iteration, k number of clusters was a value in this range. Final distortion values for each run were calculated with *scipy.cdist* (version 1.10.0) and used to construct an elbow plot from which the optimal cluster number was determined via the kneedle algorithm (*kneed* package version 0.8.1). Each centroid structure was selected by calculating the point nearest the cluster centre with the *pairwise_distances_argmin_min* method from *scikit-learn*.

Embedding coordinates for each construct were used to calculate bivariate kernel density estimations (KDEs) for both + and − trigger states and plotted as contours. The degree of overlap between + and − trigger KDEs can be used to estimate the probability of finding both states within a given cluster. Volumes for + and − trigger kernels within each cluster, and within the entire structure ensemble, were acquired by calculating the volume of an irregular solid $V = \frac{1}{2}s^2h$. Overlapping volume is determined as the sum of minimum volumes between either kernel at each position and reported as probability (P) between 0.0–1.0. Clusters that are a composite of both + and − trigger structures show high values for P while clusters that are predominantly + or − trigger have lower values.

3D modelling of UNBAR ribozymes. The FARFAR2 algorithm was utilised for de novo prediction of a given ribozyme's global fold[74]. MFE base-pair identities were supplied as secondary structure constraints to guide fragment assembly, and *-minimize_rna* was passed as an option to ensure high-accuracy modelling solutions.

Molecular dynamics preparation. FARFAR2 output was used to prepare MD simulations of trigger-bound UNBAR ribozymes. The 3D model of T-SARS-CoV-2 E-gene_Cl-29nt-clvRNA +trigger is designated as 'Native'. To produce a ribozyme model that mimics a proximal site-only cleaved state, the scissile phosphate at residue position 70 (equivalent to the canonical G + 1 site) was manually removed from the 'Native' model and prepared separately as a 'Proximal Site Cleaved' model. RNA interactions were modelled using the CHARMM36 force field[75]. All systems were solvated in a 0.1 M sodium chloride and 0.05 M magnesium chloride solution containing approximately 104,000 TIP3 water molecules. Solvation resulted in rectangular box sizes of approximately 14.5 × 14.5 × 14.5 nm.

Simulation setup. All systems were equilibrated by performing 10,000 steps of steepest descent minimisation followed by 100 ps *NpT* ensemble simulations with gradually decreasing position restraints on the RNA heavy atoms. All simulations were performed using GROMACS 2019.3 from Bekker et al.[76]. Electrostatic interactions were described using particle mesh Ewald[75]. Van-der-Waals and Ewald cutoffs were set to 1.2 nm. Bonds to hydrogen atoms were constrained with the LINCS algorithm, allowing an integration time step of 2 fs. Temperature was controlled for distinct coupling groups of solvent and solute using separate v-rescale thermostats[77] at 303.15 K, using a coupling constant τ of 1 ps. An isotropic Berendsen barostat[78] maintained a pressure of 1 atm, using a coupling constant τ of 12 ps. Following equilibration, all systems were simulated for 1,000 ns in the *NpT* ensemble. Frames were saved every 50 ps, yielding a single, continuous trajectory of 20,000 frames for each system.

Simulation analysis. All trajectories were corrected for periodicity and aligned to the reference structure using *trjconv* from the GROMACS 2019.3 package with the *-fit* and *-rot+trans* flags on. Phosphate backbone root-mean-square deviation was then calculated with *rms* and used to determine the time point at which each system reached equilibrium. Applying this time as a starting point, the conformational change of Stem B residues was evaluated with *mdmat*, and the resulting pair-wise distance matrix indicated which residue pairs undergo the largest change in distance over the course of the simulation. The pair of residues identified (positions 15 and 164) was further evaluated with *distance* to observe Stem B stability as a function of ribozyme cleavage. Three-dimensional representations were prepared with the PyMOL molecular visualisation program.

Reporting summary

Further information on research design is available in the Nature Portfolio Reporting Summary linked to this article.

Data availability

All sequences and data are available in the main text or the supplementary materials (including Supplementary Data 1). Source data are provided with this paper.

References

1. Aw, S. S., Tang, M. X., Teo, Y. N. & Cohen, S. M. A conformation-induced fluorescence method for microRNA detection. *Nucleic Acids Res.* **44**, e92 (2016).
2. Huang, K. et al. FASTmiR: an RNA-based sensor for in vitro quantification and live-cell localization of small RNAs. *Nucleic Acids Res.* **45**, e130 (2017).
3. Jin, M., Garreau de Loubresse, N., Kim, Y., Kim, J. & Yin, P. Programmable CRISPR-Cas repression, activation, and computation with sequence-independent targets and triggers. *ACS Synth. Biol.* **8**, 1583–1589 (2019).
4. Siu, K. H. & Chen, W. Riboregulated toehold-gated gRNA for programmable CRISPR-Cas9 function. *Nat. Chem. Biol.* **15**, 217–220 (2019).
5. Tang, W., Hu, J. H. & Liu, D. R. Aptazyme-embedded guide RNAs enable ligand-responsive genome editing and transcriptional activation. *Nat. Commun.* **8**, 15939 (2017).
6. Kundert, K. et al. Controlling CRISPR-Cas9 with ligand-activated and ligand-deactivated sgRNAs. *Nat. Commun.* **10**, 2127 (2019).
7. Collins, S. P., Rostain, W., Liao, C. & Beisel, C. L. Sequence-independent RNA sensing and DNA targeting by a split domain CRISPR-Cas12a gRNA switch. *Nucleic Acids Res.* **49**, 2985–2999 (2021).
8. Oesinghaus, L. & Simmel, F. C. Switching the activity of Cas12a using guide RNA strand displacement circuits. *Nat. Commun.* **10**, 2092 (2019).
9. Lin, J., Liu, Y., Lai, P., Ye, H. & Xu, L. Conditional guide RNA through two intermediate hairpins for programmable CRISPR/Cas9 function: building regulatory connections between endogenous RNA expressions. *Nucleic Acids Res.* **48**, 11773–11784 (2020).
10. Liu, Y. et al. Engineering cell signaling using tunable CRISPR-Cpf1-based transcription factors. *Nat. Commun.* **8**, 2095 (2017).
11. Liu, Y. et al. Directing cellular information flow via CRISPR signal conductors. *Nat. Methods* **13**, 938–944 (2016).
12. Ferry, Q. R., Lyutova, R. & Fulga, T. A. Rational design of inducible CRISPR guide RNAs for de novo assembly of transcriptional programs. *Nat. Commun.* **8**, 14633 (2017).
13. Lee, Y. J., Hoynes-O'Connor, A., Leong, M. C. & Moon, T. S. Programmable control of bacterial gene expression with the combined CRISPR and antisense RNA system. *Nucleic Acids Res.* **44**, 2462–2473 (2016).
14. Hanewich-Hollatz, M. H., Chen, Z., Hochrein, L. M., Huang, J. & Pierce, N. A. Conditional guide RNAs: programmable conditional regulation of CRISPR/Cas function in bacterial and mammalian cells via dynamic RNA nanotechnology. *ACS Cent. Sci.* **5**, 1241–1249 (2019).
15. Cox, K. J., Subramanian, H. K. K., Samaniego, C. C., Franco, E. & Choudhary, A. A universal method for sensitive and cell-free detection of CRISPR-associated nucleases. *Chem. Sci.* **10**, 2653–2662 (2019).
16. Wang, X. W. et al. A microRNA-inducible CRISPR-Cas9 platform serves as a microRNA sensor and cell-type-specific genome regulation tool. *Nat. Cell Biol.* **21**, 522–530 (2019).
17. Hirosawa, M. et al. Cell-type-specific genome editing with a microRNA-responsive CRISPR-Cas9 switch. *Nucleic Acids Res.* **45**, e118 (2017).
18. Hoffmann, M. D. et al. Cell-specific CRISPR-Cas9 activation by microRNA-dependent expression of anti-CRISPR proteins. *Nucleic Acids Res.* **47**, e75 (2019).
19. Lee, J. et al. Tissue-restricted genome editing in vivo specified by microRNA-repressible anti-CRISPR proteins. *RNA* **25**, 1421–1431 (2019).
20. Baccouche, A., Adel, A., Yachie, N., Fujii, T. & Genot, A. J. License to cut: smart RNA guides for conditional control of CRISPR-Cas9. Preprint at *bioRxiv*, https://doi.org/10.1101/2022.10.26.513620 (2022).
21. Zhao, E. M. et al. RNA-responsive elements for eukaryotic translational control. *Nat. Biotechnol.* **40**, 539–545 (2021).
22. Qian, Y. et al. Programmable RNA sensing for cell monitoring and manipulation. *Nature* **610**, 713–721 (2022).
23. Kaseniit, K. E. et al. Modular, programmable RNA sensing using ADAR editing in living cells. *Nat. Biotechnol.* **41**, 482–487 (2022).
24. Jiang, K. et al. Programmable eukaryotic protein synthesis with RNA sensors by harnessing ADAR. *Nat. Biotechnol.* **41**, 698–707 (2022).
25. Ono, H. & Saito, H. Sensing intracellular signatures with synthetic mRNAs. *RNA Biol.* **20**, 588–602 (2023).
26. Lee, R. T., Ng, A. S. & Ingham, P. W. Ribozyme mediated gRNA generation for in vitro and in vivo CRISPR/Cas9 mutagenesis. *PLoS ONE* **11**, e0166020 (2016).
27. Gao, Y. & Zhao, Y. Self-processing of ribozyme-flanked RNAs into guide RNAs in vitro and in vivo for CRISPR-mediated genome editing. *J. Integr. Plant Biol.* **56**, 343–349 (2014).
28. Litke, J. L. & Jaffrey, S. R. Highly efficient expression of circular RNA aptamers in cells using autocatalytic transcripts. *Nat. Biotechnol.* **37**, 667–675 (2019).

29. Zhong, G. et al. A reversible RNA on-switch that controls gene expression of AAV-delivered therapeutics in vivo. *Nat. Biotechnol.* **38**, 169–175 (2020).
30. Lindley, S. R. et al. Ribozyme-activated mRNA trans-ligation enables large gene delivery to treat muscular dystrophies. *Science* **386**, 762–767 (2024).
31. Strack, R. L., Disney, M. D. & Jaffrey, S. R. A superfolding Spinach2 reveals the dynamic nature of trinucleotide repeat-containing RNA. *Nat. Methods* **10**, 1219–1224 (2013).
32. Paige, J. S., Wu, K. Y. & Jaffrey, S. R. RNA mimics of green fluorescent protein. *Science* **333**, 642–646 (2011).
33. Shippy, R., Lockner, R., Farnsworth, M. & Hampel, A. The hairpin ribozyme. Discovery, mechanism, and development for gene therapy. *Mol. Biotechnol.* **12**, 117–129 (1999).
34. Walter, N. G. & Burke, J. M. The hairpin ribozyme: structure, assembly and catalysis. *Curr. Opin. Chem. Biol.* **2**, 303 (1998).
35. Perez-Ruiz, M., Barroso-DelJesus, A. & Berzal-Herranz, A. Specificity of the hairpin ribozyme. Sequence requirements surrounding the cleavage site. *J. Biol. Chem.* **274**, 29376–29380 (1999).
36. Hampel, A. & Tritz, R. RNA catalytic properties of the minimum (-) sTRSV sequence. *Biochemistry* **28**, 4929–4933 (1989).
37. Schmidt, C., Welz, R. & Muller, S. RNA double cleavage by a hairpin-derived twin ribozyme. *Nucleic Acids Res.* **28**, 886–894 (2000).
38. Welz, R. et al. Site-directed alteration of RNA sequence mediated by an engineered twin ribozyme. *Angew. Chem. Int. Ed.* **42**, 2424–2427 (2003).
39. Pinard, R., Lambert, D., Pothiawala, G., Major, F. & Burke, J. M. Modifications and deletions of helices within the hairpin ribozyme-substrate complex: an active ribozyme lacking helix 1. *RNA* **10**, 395–402 (2004).
40. Kuzmin, Y. I., Da Costa, C. P., Cottrell, J. W. & Fedor, M. J. Role of an active site adenine in hairpin ribozyme catalysis. *J. Mol. Biol.* **349**, 989–1010 (2005).
41. Salter, J., Krucinska, J., Alam, S., Grum-Tokars, V. & Wedekind, J. E. Water in the active site of an all-RNA hairpin ribozyme and effects of Gua8 base variants on the geometry of phosphoryl transfer. *Biochemistry* **45**, 686–700 (2006).
42. Liu, L., Cottrell, J. W., Scott, L. G. & Fedor, M. J. Direct measurement of the ionization state of an essential guanine in the hairpin ribozyme. *Nat. Chem. Biol.* **5**, 351–357 (2009).
43. Nam, K., Gao, J. & York, D. M. Quantum mechanical/molecular mechanical simulation study of the mechanism of hairpin ribozyme catalysis. *J. Am. Chem. Soc.* **130**, 4680–4691 (2008).
44. Daher, M., Mustoe, A. M., Morriss-Andrews, A., Brooks, C. L. & Walter, I. I. I. N.G. Tuning RNA folding and function through rational design of junction topology. *Nucleic Acids Res.* **45**, 9706–9715 (2017).
45. Yadava, R. S., Choi, A. J., Lebruska, L. L. & Fedor, M. J. Hairpin ribozymes with four-way helical junctions mediate intracellular RNA ligation. *J. Mol. Biol.* **309**, 893–902 (2001).
46. Mlynsky, V. et al. Extensive molecular dynamics simulations showing that canonical G8 and protonated A38H+ forms are most consistent with crystal structures of hairpin ribozyme. *J. Phys. Chem. B* **114**, 6642–6652 (2010).
47. Siwkowski, A., Shippy, R. & Hampel, A. Analysis of hairpin ribozyme base mutations in loops 2 and 4 and their effects on cis-cleavage in vitro. *Biochemistry* **36**, 3930–3940 (1997).
48. Soukup, G. A. & Breaker, R. R. Engineering precision RNA molecular switches. *Proc. Natl. Acad. Sci. USA* **96**, 3584–3589 (1999).
49. Soukup, G. A., Emilsson, G. A. & Breaker, R. R. Altering molecular recognition of RNA aptamers by allosteric selection. *J. Mol. Biol.* **298**, 623–632 (2000).
50. Zhu, J., Hieronymus, R. & Muller, S. A hairpin ribozyme derived spliceozyme. *Chembiochem* **24**, e202300204 (2023).
51. Rupert, P. B., Massey, A. P., Sigurdsson, S. T. & Ferre-D' Amare, A. R. Transition state stabilization by a catalytic RNA. *Science* **298**, 1421–1424 (2002).
52. Li, X. et al. Imaging intracellular S-adenosyl methionine dynamics in live mammalian cells with a genetically encoded red fluorescent RNA-based sensor. *J. Am. Chem. Soc.* **142**, 14117–14124 (2020).
53. Drude, I., Strahl, A., Galla, D., Muller, O. & Muller, S. Design of hairpin ribozyme variants with improved activity for poorly processed substrates. *FEBS J.* **278**, 622–633 (2011).
54. Pasquinelli, A. E. et al. Conservation of the sequence and temporal expression of let-7 heterochronic regulatory RNA. *Nature* **408**, 86–89 (2000).
55. Bosson, A. D., Zamudio, J. R. & Sharp, P. A. Endogenous miRNA and target concentrations determine susceptibility to potential ceRNA competition. *Mol. Cell* **56**, 347–359 (2014).
56. Janas, M. M. et al. Alternative RISC assembly: binding and repression of microRNA-mRNA duplexes by human Ago proteins. *RNA* **18**, 2041–2055 (2012).
57. Filonov, G. S., Moon, J. D., Svensen, N. & Jaffrey, S. R. Broccoli: rapid selection of an RNA mimic of green fluorescent protein by fluorescence-based selection and directed evolution. *J. Am. Chem. Soc.* **136**, 16299–16308 (2014).
58. Wei, C., Salichos, L., Wittgrove, C. M., Rokas, A. & Patton, J. G. Transcriptome-wide analysis of small RNA expression in early zebrafish development. *RNA* **18**, 915–929 (2012).
59. Tian, T., Zhao, L., Zhao, X., Zhang, M. & Meng, A. A zebrafish gene trap line expresses GFP recapturing expression pattern of foxj1b. *J. Genet. Genom.* **36**, 581–589 (2009).
60. de Jong, O. G. et al. A CRISPR-Cas9-based reporter system for single-cell detection of extracellular vesicle-mediated functional transfer of RNA. *Nat. Commun.* **11**, 1113 (2020).
61. Romani, A.M.P. (eds Vink, R. & Nechifor, M.) *Magnesium in the Central Nervous System* (Adelaide, 2011).
62. Yan, D. H. et al. Different intracellular polyamine concentrations underlie the difference in the inward rectifier K(+) currents in atria and ventricles of the guinea-pig heart. *J. Physiol.* **563**, 713–724 (2005).
63. Watanabe, S., Kusama-Eguchi, K., Kobayashi, H. & Igarashi, K. Estimation of polyamine binding to macromolecules and ATP in bovine lymphocytes and rat liver. *J. Biol. Chem.* **266**, 20803–20809 (1991).
64. Berzal-Herranz, A., Joseph, S., Chowrira, B. M., Butcher, S. E. & Burke, J. M. Essential nucleotide sequences and secondary structure elements of the hairpin ribozyme. *EMBO J.* **12**, 2567–2573 (1993).
65. Joseph, S. & Burke, J. M. Optimization of an anti-HIV hairpin ribozyme by in vitro selection. *J. Biol. Chem.* **268**, 24515–24518 (1993).
66. Welz, R., Schmidt, C. & Muller, S. Spermine supports catalysis of hairpin ribozyme variants to differing extents. *Biochem. Biophys. Res. Commun.* **283**, 648–654 (2001).
67. Madeo, F., Eisenberg, T., Pietrocola, F. & Kroemer, G. Spermidine in health and disease. *Science* **359**, eaan2788 (2018).
68. Xiang, J. S. et al. Massively parallel RNA device engineering in mammalian cells with RNA-Seq. *Nat. Commun.* **10**, 4327 (2019).
69. Felletti, M., Stifel, J., Wurmthaler, L. A., Geiger, S. & Hartig, J. S. Twister ribozymes as highly versatile expression platforms for artificial riboswitches. *Nat. Commun.* **7**, 12834 (2016).
70. Warren, L. et al. Highly efficient reprogramming to pluripotency and directed differentiation of human cells with synthetic modified mRNA. *Cell Stem Cell* **7**, 618–630 (2010).
71. Stewart, S. A. et al. Lentivirus-delivered stable gene silencing by RNAi in primary cells. *RNA* **9**, 493–501 (2003).
72. Reuter, J. S. & Mathews, D. H. RNAstructure: software for RNA secondary structure prediction and analysis. *BMC Bioinform.* **11**, 129 (2010).

73. Ding, Y., Chan, C. Y. & Lawrence, C. E. Clustering of RNA secondary structures with application to messenger RNAs. *J. Mol. Biol.* **359**, 554–571 (2006).
74. Watkins, A. M., Rangan, R. & Das, R. FARFAR2: improved de novo Rosetta prediction of complex global RNA folds. *Structure* **28**, 963–976 e966 (2020).
75. Huang, J. & MacKerell, A. D. Jr CHARMM36 all-atom additive protein force field: validation based on comparison to NMR data. *J. Comput. Chem.* **34**, 2135–2145 (2013).
76. Bekker, H. et al. Gromacs: a parallel computer for molecular dynamics simulations. *Phys. Comput.* **92**, 252–256 (1993).
77. Bussi, G., Donadio, D. & Parrinello, M. Canonical sampling through velocity rescaling. *J. Chem. Phys.* **126**, 014101 (2007).
78. Parrinello, M. A. R., A. Polymorphic transitions in single crystals: a new molecular dynamics method. *J. Appl. Phys.* **52**, 7182–7190 (1981).

Acknowledgements

We would like to thank Dr. Jong, O.G. de Olivier and Dr. Pieter Vader for generously sharing the HEK293T Stoplight+ spCas9+ cells, and Dr. Yan Chuan for sharing HEK293T cells. Several constructs were obtained from Addgene. We would like to thank Ah Keng Chew for technical assistance on DNA fragment analyses, Enjun Yang, Daniel Silva and the flow core facility for help on flow cytometry and analyses, and members of the Aw Lab, Tommaso Tabaglio, Paolo Pigini, Polly Chen and Jackie Ying for helpful discussions and comments on the manuscript. We would also like to thank Leslie Beh, Joy Xiang and Farid Ghadessy for their thoughtful comments on the manuscript. We thank Dr. Daniel Ackerman of Insight Editing London for editing this manuscript prior to submission. Funding for this study was provided by: National Medical Research Council Young Individual Research Grant (NMRC OFYIRG16-may045 to S.S.A.), A*STAR Biomedical Research Council Central Research Fund Use-Inspired Basic Research (to S.S.A.), A*STAR Career Development Award (to M.L.), A*STAR Industry-Alignment Fund Pre-Positioning grant (H20C6a0034 to S.A. and D.W.), ESCO-Ventures-Enterprise Platinum grant (ACVC/20-AVC001-A20; EVX_TX009 to S.A.) and A*STAR Cell and Gene Therapy Flagship Grant (C253623010 to S.A.) and IMCB, A*STAR core funding (to S.R.).

Author contributions

S.S.A., M.L., C.T. and C.S.S. conceptualised the study and analysed the data. M.L., C.T., C.S.S., S.J.T., S.K.P., S.L., C.H.K., D.R. and J.C. performed experiments and analysed the data. L.F.J. performed molecular modelling and the associated data analysis and data visualisation. D.W., S.R., R.H. and S.S.A. supervised the study. S.S.A. prepared the original draft, and all authors reviewed or edited the draft.

Competing interests

S.S.A., M.L., C.T., C.S.S., S.J.T., S.K.P. and C.H.K. are inventors on patent applications related to the ribozymes described in this paper. The remaining authors declare no competing interests.

Additional information

Supplementary information The online version contains supplementary material available at https://doi.org/10.1038/s41467-025-68175-5.

Correspondence and requests for materials should be addressed to Sherry Shiying Aw.

Peer review information *Nature Communications* thanks the anonymous reviewer(s) for their contribution to the peer review of this work. A peer review file is available.